Bull. Soc. géol. Fr., 2002, t. 173, n° 6, pp. 491-508

Cartography of the Ronda peridotite (Spain) by hyperspectral remote sensing

PATRICK LAUNEAU[1], CHRISTOPHE SOTIN[1] and JACQUES GIRARDEAU[1]

Key words. – Ronda, Peridotite, Petrography, Hyperspectral, SAM, AVIRIS

Abstract. – The Ronda Peridotite, south of Andalusia (Spain), was imaged by AVIRIS in 1991 and partially sampled by us in the field with a GER 3700 spectrometer in 1997 in order to get experience in processing hyperpectral images of planetary surfaces with probes such as ISM Phobos (1989), OMEGA Mars Express (2003) and VIMS Cassini (2004). The high spectral resolution of the images (224 channels from 400 to 2455 nm) is necessary to conduct geological analysis with remote petrological determinations of rock types. On Earth, it is also necessary to determine species of vegetation because of their strong influence in mapping lithology, even in dry areas like the Ronda peridotite.

The Ronda AVIRIS image was first processed to infer geological features using photo-interpretation of colour composite images extracted from 150 useful channels compared to geological maps and checked on the field during the campaign of July 97. This allows us to distinguish easily the peridotite massif from its surrounding rocks and its own serpentine zoning.

Since this work followed the work of Chabrillat *et al.* [2000] we chose to explore the AVIRIS data with other techniques. We chose to remove the contribution of the atmosphere with spectra collected in the field on a white target at various altitudes and to remove the main vegetation with spectra of the most characteristic vegetation of the peridotite. In both cases we first estimated the amount of atmosphere and vegetation with band ratios and remove them with two similar empiric corrections of the reflectance.

From the spectroscopy data, after removal of the atmosphere and some vegetation signal, we were able to clearly distinguish the crustal rocks from the mantle ones, as well as compositional variations due to pyroxene and mostly serpentine abundance within the peridotites. Hyperspectral infrared spectrometry will provide good geological mapping of the main rocks on planetary surfaces, if images can also be calibrated with in situ field measurements which will not miss any unexpected component. However, some ambiguities remain between certain types of rock which have close mineralogical composition (e.g. harzburgite compared to lherzolite) or which have resulting spectra very similar to each other (plagioclase and lizardite in peridotites). Some other ambiguities between spectra are also introduced by techniques of analysis based on relative reflectance. By not taking into account absolute intensity of the reflectance, because of roughness and topographic shading effects, small mineral variations are not always visible.

Cartographie de la péridotite de Ronda (Espagne) par télédétection hyperspectrale : données AVIRIS

Mots clés. – Ronda, Péridotite, Pétrographie, Hyperspectral, SAM, AVIRIS

Résumé. – La péridotite de Ronda, au sud de l'Andalousie (Espagne), a été imagée par AVIRIS en 1991 et partiellement échantillonnée par nous-même sur le terrain à l'aide d'un spectromètre GER 3700 en 1997 dans le but d'acquérir une expérience dans le traitement des images hyperspectrales des surfaces planétaires à l'aide de sondes telle que ISM Phobos (1989), OMEGA Mars Express (2003) and VIMS Cassini (2004). La haute résolution spectrale des images (224 canaux répartis entre 400 et 2 455 nm) est nécessaire à la conduite d'une analyse géologique avec identification à distance des faciès pétrologiques. Sur Terre, il est aussi nécessaire de déterminer les espèces végétales à cause de leur grande influence sur la cartographie des faciès pétrologiques, même dans des régions relativement arides comme celle de la péridotite de Ronda. Cependant, la péridotite de Ronda reste un bon site test.

L'image AVIRIS de Ronda est d'abord analysée par photo-interprétation. Des compositions colorées (affichées sur les canaux rouge, vert et bleu visibles) sont construites à partir de 3 canaux visibles et/ou infrarouge choisis parmi les 150 canaux utiles (le dernier détecteur AVIRIS ne fonctionnant pas en 1991). Ces compositions colorées permettant de visualiser les principales caractéristiques géologiques du visible à l'infrarouge, il est alors possible de les comparer à des cartes géologiques, puis aux mesures de terrain de la campagne de juillet 1997. Cette analyse visuelle permet de distinguer très facilement le massif de péridotite de ses roches avoisinantes (gneiss, marbres, grès et calcaires) ainsi que de mettre en évidence une nette zonation en serpentine habituellement non cartographiée.

Ce travail faisant suite à celui de Chabrillat *et al.* [2000] nous avons pris le parti d'explorer une autre voie que celle des analyses en composantes principales en cherchant à retirer couche par couche les différents éléments à l'origine de la réponse spectrale de la péridotite de Ronda. Nous avons aussi pris le parti de ne nous fier qu'aux mesures de terrain et de ne jamais avoir recours à des échantillons d'image pour effectuer des classifications car notre expérience du terrain nous a clairement montré qu'aucun pixel n'était constitué d'une seule composante à 100 %.

[1]UMR-CNRS 6112, Planétologie et Géodynamique, Université de Nantes, Faculté des Sciences et des Techniques, 2 rue de la Houssinière, 44322 Nantes France. Patrick.Launeau@chimie.univ-nantes.fr; Christophe.Sotin@chimie.univ-nantes.fr; Jacques.Girardeau@chimie.univ-nantes.fr
Manuscrit déposé le 29 octobre 2001 ; accepté après révision le 30 avril 2002.

Parmi les couches d'éléments entrant dans la formation d'un spectre, il y a d'abord l'atmosphère et la végétation. Nous avons retiré la contribution de l'atmosphère de façon empirique en estimant sa contribution par l'analyse du rapport spectral (AF) entre des références blanches (spectralon®) mesurées sur le terrain au sommet (1400 m) et au pied de la péridotite (350 m). Un modèle numérique de terrain est construit à partir de cette détection de l'épaisseur de l'atmosphère autour de la bande de la vapeur d'eau à 940 nm et comparé à une carte topographique pour contrôler la qualité de cette détection. Il suffit alors de diviser le spectre par une fraction de AF proportionnelle à l'épaisseur de l'atmosphère. Suivant le même principe, il est possible d'utiliser le spectre de la végétation moyenne couvrant la péridotite pour retirer sa contribution, pourvu que celle-ci ne dépasse pas 40 %. Grâce à ces deux corrections (atmosphère, végétation moyenne), nous avons pu clairement distinguer roches crustales et roches mantelliques ainsi que quelques variations de teneurs en pyroxènes. Mais c'est la serpentine qui a donnée les meilleurs résultats, notamment avec la lizardite blanche.

Si toute la péridotite est le plus souvent serpentinisée, il est remarquable de constater que la lizardite s'est plutôt développée dans des failles tardives caractéristiques d'une tectonique extensive alors que le chrysotile s'est préférentiellement développé dans les failles de compression. La lizardite est blanche et le chrysotile vert et tous les deux s'assombrissent en fonction de leur teneur en magnétite. Comme la magnétite est souvent concentrée dans la lizardite en petits filonets, la signature de cette lizardite est très blanche, ce qui la rend extrêmement difficile à distinguer des plagioclases dans le domaine de longueur d'onde disponible de 440 à 1800 nm. Comme pour le plagioclase, la détection des autres minéraux de classification des faciès de la péridotite de Ronda n'a pas été possible en raison de leur trop faible pourcentage modal au regard des fortes variations modales en olivine, pyroxènes, serpentines et magnétite.

La spectrométrie infrarouge hyperspectrale devrait donc permettre de réaliser de bonnes cartes géologiques des principales roches des surfaces planétaires, mais seulement si l'image peut être calibrée par des mesures de terrain in-situ qui seules, à l'opposé des modèles, n'oublierons pas de prendre en compte toutes les composantes, même les plus inattendues. Des ambiguïtés resteront toujours présentes entre certains faciès pétrologiques de composition proche (comme harzburgite et lherzolite) ou qui présentent des spectres semblables les uns aux autres (comme pour les péridotites à plagioclase ou à lizardite entre 440 et 1 800 nm). D'autres ambiguïtés entre spectres sont encore introduites par l'emploi de méthodes d'analyse utilisant des mesures relatives de réflectance. En effet, la non prise en compte des intensités de réflectance absolue, pour éviter les effets d'ombrage de rugosité des surfaces et de leur topographie, peut entraîner une mauvaise détection de faibles variations minéralogiques.

INTRODUCTION

The Earth peridotite massifs are of great interest for planetary geology because they show the mantle part of planets that potentially may locally outcrop at their surface and therefore be recognised directly by visible-infrared (VIR) spectroscopy remote sensing. The Ronda peridotite (Spain) is one of the well-known Earth massifs that was considered as suitable for VIR spectroscopy because of its limited amount of vegetation cover. It was therefore imaged by AVIRIS (Air Borne Visible InfraRed Imaging Spectrometer) in May 1991 during the Europe Airborne Campaign of the NASA-ER2 plane and re-sampled in July 1997 with a GER 3 700 hand-spectrometer with 680 channels in the same range of wavelength as AVIRIS to calibrate the remote sensing data on the ground.

The Ronda peridotite : petrographical features

The Ronda peridotite massif outcrops in the southern part of Spain, in Andalousia, at the latitude of about N036° in a Mediterranean climate (fig. 1a). It is a slice of mantle that was uplifted during Alpine orogeny [Sánchez-Rodríguez and Gebauer, 2000]. The massif is now in tectonic contact with continental metamorphic series of the Betic Cordilleras that dominantly comprise metapelitic rocks (gneisses and schists) and marbles of Paleozoic to Triassic ages (see precise descriptions of these lithologies in Tubía *et al.* [1986, 1992, 1997]).

This peridotite massif is mainly composed of plagioclase and spinel lherzolites with subordinate (less than 10 %) dunites, harzburgites, garnet-bearing lherzolites and various types of pyroxenites [Lundeen and Obata, 1977 ;

FIG. 1. – ***a–*** Geological map (after Lundeen and Obata [1977], modified by Tubía, personal comminucation). Pzb : Blanca Unit, Pzc and SOm : Casares Unit, CDm : Malaguide complex, To : Oligocene sandstone, GL : Garnet Lherzolite, SL : Spinel Lherzolite, PL : Plagioclase Lherzolite, red lines : faults; ***b***– Olivine distribution [after Darot, 1973] : yellow 65-80 %, light green 80-85 % and dark green 85-100 %, red lines : road, blue lines : streams; ***c***– Colour composite image enhancing vegetation (deciduous tree : light green, conifers : dark green, grass land and bushes : faded green), serpentine content in peridotite (light to medium violet, see detail in ***e***) and burnt area (purple). Geological boundaries are drawn in black from colour composite images; ***d***– Colour composite image of the minimum, mean and maximum reflectance calculated for each pixel between 440 nm and 1800 nm. Peridotite and gneiss are orange, sandstone light yellow, forest blue (light blue for broad-leafed trees and dark blue for conifers) and forest fire area red. ***e–*** Subset of the AVIRIS image showing details of contact between rock types : peridotite – serpentine-rich peridotite – sandstone. ***f***– Same subset enhancing other rock types (see text for discussion). ***g***– Detail showing the sub-pixel geometry of the outcrop. Note also the thickness of the pyroxenite layer. ***h***– Picture of the Ronda massif near the top of Los Reales mountain, looking toward the Mediterranean sea showing outcrops with various roughness and vegetation covers. ***i***– Centre of the peridotite massif (centre of row # 512, ***d***) showing a crest bounded by a pine forest.

FIG. 1. – ***a–*** *Carte géologique (d'après Lundeen et Obata [1977], modifié par Tubía, communication personnelle).* Pzb *: unité de Blanca,* Pzc *et* SOm *: unité de Casares, CDm : complexe de Malaguide,* To *: Grès Oligocène,* GL *: lherzolite à grenat, ligne rouge : failles;* ***b–*** *Distribution de l'olivine [d'après Darot, 1973] : jaune 65-80 %, vert clair 80-85 % et vert foncé 85-100 %, le réseau routier est en rouge, hydrographique en bleu;* ***c–*** *Composition colorée mettant en évidence la végétation (feuillus en vert clair, conifères en vert foncé, prairie et taillis en vert pâle), la teneur de la péridotite en serpentine (violet clair à moyen, voir détail en e) et zone brûlée (pourpre). Les frontières entre formations géologiques dessinées à partir des compositions colorées sont en trait noir;* ***d–*** *Composition colorées des réflectances minimum, moyenne et maximum, calculées pour chaque pixel entre 440 nm et 1800 nm. Péridotite et gneiss sont orange, les grès jaune clair, les forêts sont bleu (bleu clair pour les feuillus et bleu foncé pour les conifères) et la forêt brûlée est rouge.* ***e–*** *agrandissement d'un extrait de l'image AVIRIS montrant en détail le contact entre les roches suivantes : péridotite – péridotite riche en serpentine – grès.* ***f–*** *Même agrandissement mettant en évidence d'autre variation lithologiques (voir texte pour discussion).* ***g–*** *Détail montrant la géométrie d'un affleurement à l'échelle sub-pixel. Remarquez aussi l'épaisseur du lit de pyroxénite.* ***h–*** *Photographie du massif de Ronda près du mont Los Reales en regardant vers la Méditerranée, montrant différentes rugosité d'affleurement et différentes couvertures végétales.* ***i–*** *Autre photographie du centre du massif de péridotite (au centre de la ligne n° 512,* ***d****) montrant la couverture végétale le long d'une crête bordée par une forêt de pins.*

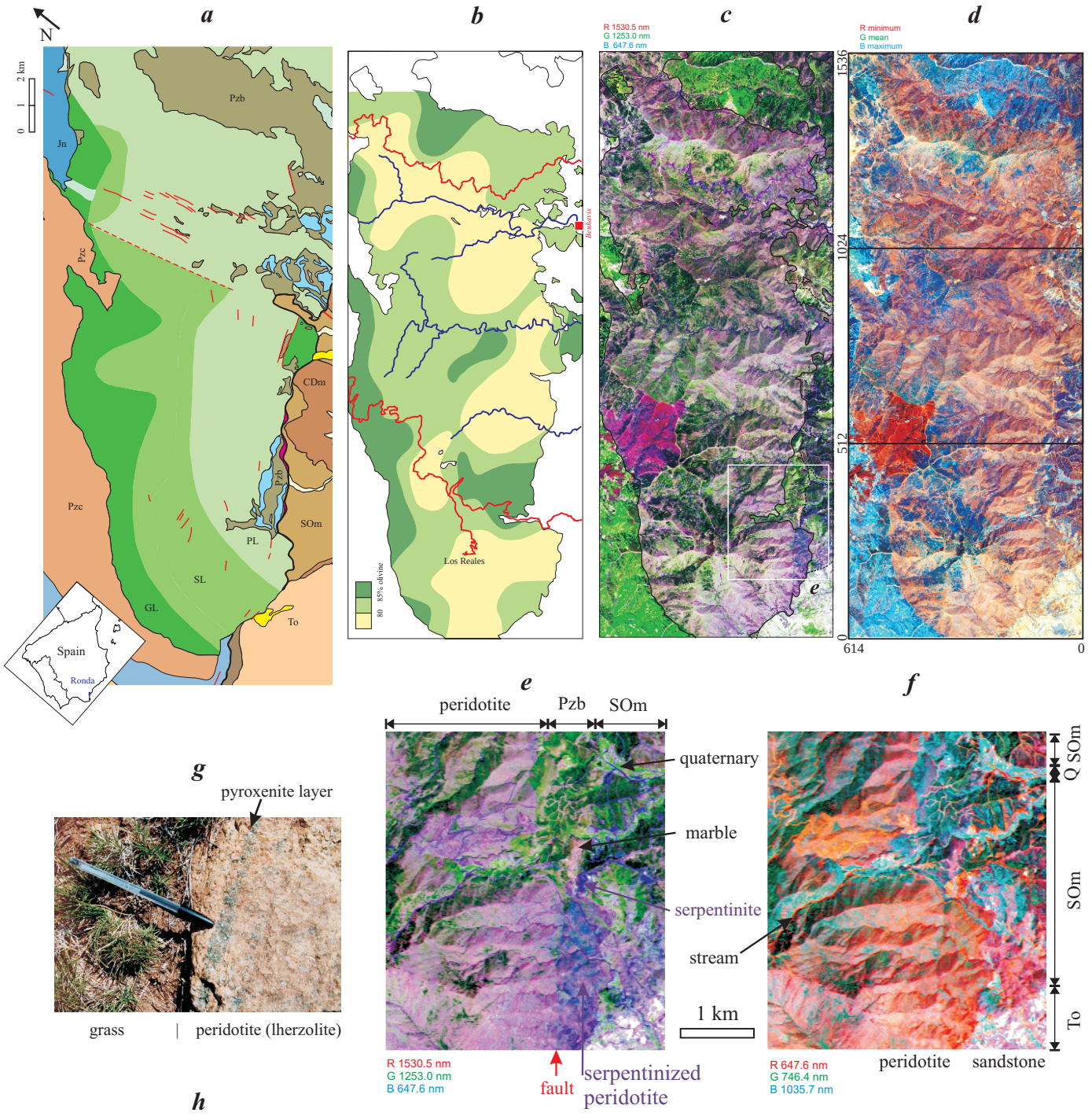
a
N
0 1 2 km
Pzb
Jn
Pzc
CDm
Pzb
Pzc
SOm
PL
SL
GL
To
Spain
Ronda
b
Los Reales
80 85% olivine
c
R 1530.5 nm
G 1253.0 nm
B 647.6 nm
e
d
R minimum
G mean
B maximum
1536
1024
512
0
614
0
e
peridotite
Pzb
SOm
quaternary
marble
serpentinite
stream
1 km
R 1530.5 nm
G 1253.0 nm
B 647.6 nm
fault
serpentinized peridotite
f
Q SOm
SOm
To
peridotite
sandstone
R 647.6 nm
G 746.4 nm
B 1035.7 nm
g
pyroxenite layer
grass
peridotite (lherzolite)
h
i

Obata, 1980]. Hence, the main mineral phase of the Ronda peridotite massif is olivine, of which the modal composition varies from more than 90 % in dunites down to 65 % in lherzolites. However, 30 to 90 % of this primary mineral is now transformed into serpentines and magnetite, following the post-emplacement-related hydration of the olivine structure and concomitant concentration of Fe in opaque inclusions. Petrographical studies by Darot [1973] have shown that the olivine distribution at the massif scale is heterogeneous (fig. 1b). The second mineral phases of the Ronda peridotite are pyroxenes which can be divided into clinopyroxene and orthopyroxene, equally distributed within the lherzolites where their overall amount is always below 30 %, with a mean value around 20 %. In the harzburgites, the orthopyroxene content can reach 20 % modal content and clinopyroxene 5 to 10 % ; it is absent in the dunites. The modal content of all the other phases present in these peridotites is always very low : around 1 % to 4 % for plagioclase, between 1 and 3 % for spinel and less than 1 % for garnet when present, i.e. at the uppermost part of the sheet along the northern mantle-crust boundary. Because of their petrological and geodynamical significance, the presence of these three aluminous phases has been used to define the 3 main types of peridotite mapped by geologists. But there is no clear correlation between the lithological limits defined with aluminous phases (fig. 1a) and the olivine distribution on the whole massif (fig. 1b).

The Ronda peridotite also locally comprises layers 10 cm to 2 m thick of pyroxenites and of rare olivine gabbros that generally stand subparallel to the main foliation within the peridotites like in many other peridotite massifs [Nicolas, 1986]. These pyroxenites contain up to 80 % of pyroxenes, mostly clinopyroxenes, with some plagioclase, olivine and spinel. The peridotite is also locally cross cut by very rare and late granitic intrusions which formed during the latest stages of uplift of the peridotites [Tubía *et al*., 1997]. All these subordinate lithologies, scattered within the whole peridotite, represent less than 5 % of the Ronda massif.

In the field, the peridotite can be easily identified beneath the vegetation, grass or trees (fig. 1g to 1i). Most of the peridotite outcrops indeed display a characteristic oxidized yellow to red skin, at the origin of its Sierra Bermeja (reddish mountains) local name, whereas it can be dark green or brown on fresh sections. Field observations indicate that the reddish outcrops are often pathways of old forest fires that have favored the formation of hematite. At the sample scale, we can distinguish easily on the yellow to reddish background grey-brown centimeter-size orthopyroxene and smaller sized light grey-green clinopyroxene (fig. 1g). Millimeter-size black spinels, with locally tiny rims of white plagioclase, can be also recognized on these backgrounds. Because of its dark red or medium brown colour resembling the orthopyroxene, and also because of its scarcity and small size, garnet is very difficult to identify in the field [Obata, 1980]. The massive serpentinized peridotite which represents the most common facies has light grey patinas and is dark inside when rich in magnetite. This is due to a common thin skin of alteration that washed out the magnetite on most outcrops. Some other serpentinites from veins or late shear zones are light green to white, being mostly free of magnetite. All these partially serpentinized peridotites can be locally covered by a thin yellow-green to red soil, final product of the weathering action. The yellow-green colour is due to a pyroxene sand, whereas the red colour is due to oxidised iron-rich soils.

It is clear from these petrographic descriptions that a geologist familiar with mantle rocks can map most of these small-scale petrological variations as shown on figure 1a and 1b. But it is also clear that such mapping requires careful observations of the rocks by the geologist to identify the rock type and distribution. So why look at such peridotites from an airborne device and why with AVIRIS ? First, because we consider that such work using high-resolution spectrometer represents a good training study for planetary remote sensing (VIMS on Cassini-Huygens, ISM on Phobos, OMEGA on Mars-Express) as well as for other Earth studies for which field outcrops are difficult to reach. Second, because remote sensing gives the right scale to map huge geological features. This last reason explains why airphotos and satellite images (for instance Spot, Landsat and others) have been largely used for a few decades to map some large-scale tectonic structures like folds and faults [e.g. Richards J. A., 1994]. However, they all use only a few channels collecting the light in large spectral windows. With imaging spectrometers like AVIRIS, we have access to more than 200 channels in narrow bands, between 0.4 and 2.4 μm, providing a denser representation of spectrum for each 20 m × 20 m pixel. This potentially allows the determination of minerals and rocks with spectroscopic techniques. Of course, the size of each pixel implies a mixing of spectrum of minerals and vegetation in such a way that clear identification may be very difficult. To resolve this problem, one can compare a pixel spectra of rock with laboratory and field measurements, or one can also model it, using spectrum of minerals and plant species. Both methods have to be used but we will focus the present study on the comparison with field spectra.

Data processing

AVIRIS has 224 channels between 400 nm and 2 455 nm [Vane *et al*., 1993]. A full spectrum is stored for each pixel. In addition, we acquired 700 new spectra from 34 different sites during a field campaign in July 1997. For these measurements, we use a GER 3700 spectrometer with 680 channels in the same wavelength range. Because of technical problems (detector D broke down) our AVIRIS data cannot be analysed over 1800 nm, so we limit this study to a 400 to 1 800 nm range (150 AVIRIS channels).

In this paper, we first analyse the raw AVIRIS data on colour composite images made of any 3 channels among the 150 available. This step, often neglected in studies of spectrometry, is in fact necessary to understand the real meaning of any spectrum as it will be shown for the case of the forest fire area (fig. 1c and 1d). We were able to outline the main geological boundaries between gneiss, marbles and peridotite, easily separated from one another because of their own colours, but most of all, because of the variation of their vegetation covers. More subtle variations have been mapped, like the presence of serpentine along a major fault which was not completely identified before (compare with Van Der Wal [1993, 1996] and Sánchez-Gómez *et al.* [1995] for example). This photo interpretation work was indeed very useful to setup our field campaign of 1997 and to locate the best sites for spectroscopy measurements.

Calibration of the image was carried out with a classical empirical line correction using AVIRIS and GER 3700 data. We also calculated a digital elevation model based on the intensity of the water vapour absorption feature at 940 nm following the work of Green *et al*. [1989], Gao *et al*. [1993] and Roberts *et al*. [1997]. We were therefore able to remove the atmospheric overprint with an empirical function given by the ratio of the radiance measured on a piece of Spectralon®, at the bottom and at the top of the peridotite, the same day just before and after noon. The image was then analysed using simple calculations of distance between field spectra re-sampled to fit the AVIRIS spectrum. Like Van de Meer [1996] we basically looked at the correlation coefficient between spectra using the Spectral Angle Mapper (SAM) as presented by Kruse *et al.* [1993]. However, because of the grass abundance over the peridotite, we removed the grass signal with an algorithm similar to the empirical atmosphere correction. The meaning of these analyses was then discussed.

For those who are reluctant to use photo interpretation in modern analysis, we would like to recall here that it is a strong and efficient way to identify the main components of an image and avoid strong artefacts (see fire forest comments in the photo-interpretation section, fig. 1c et 1d). We show in this paper (see atmosphere removal section) that the atmosphere component should and can be removed on old images, even six or ten years after their acquisition (see comparison between atmosphere thickness and topography in fig. 6 j and 6 k). We also show that it is important for geological studies to consider the variability of the vegetation over different lithologies, which can induce misleading interpretation of the lithology when it is not correctly removed (see vegetation removal section).

Complementary analyses

This work is also a complementary analysis of the Chabrillat *et al.* [2000] study of the same AVIRIS data. They have explored spectral mixing analysis (SMA) and have used principal component analysis to identify end members and RMS techniques to map their relative abundance. Our approach is different. Instead of trying to "unmix" the spectra of various substances, we first try to remove one at a time, all the components that can be identified (atmosphere, vegetation cover). From our point of view, the end members fractions presented by Chabrillat *et al.* [2000] in figure 7 are mixed with a fraction of atmosphere and vegetation. For instance, this is shown by their end members map of the Los Reales mountain peridotite [Chabrillat *et al*., 2000, fig. 7c] which fit well with the water vapour absorption band (940 nm channel, fig. 6-a, this work). We hence consider that any process should start by the removal of some image components like atmosphere, including its variation with altitude, or a specific vegetation which are both presented in this work.

PHOTO INTERPRETATION

Raw data and false colour output

As can be seen on raw spectral data in figure 2a, the atmosphere is mainly responsible for the pattern of the average spectra, and particularly with the usual H_2O and CO_2 absorption bands. They not only reduce the relative brightness of the whole image but they also shrink the data range of intensity. This is well demonstrated in figure 2a by the distance between curves of mean plus or minus 4 times the standard deviation ($+4\sigma$ and -4σ, fig. 2a). The largest distance between minimum and maximum raw intensities ($\approx 8\sigma$) is 280 at 1 050 nm whereas it is only 40 at 1 150 nm. Narrow levels of information are thus more sensitive to noise and not suitable for photo-interpretation. As usual in image analysis, we send 3 given channels on the red, green and blue channel of a monitor to display false colour composite images (see fig. 1c and 1e). The levels of each channel are then adjusted to the output of the screen with respect to their mean value. This effect is presented in figure 2b, the mean values draw a straight line. It is also known as the "in-

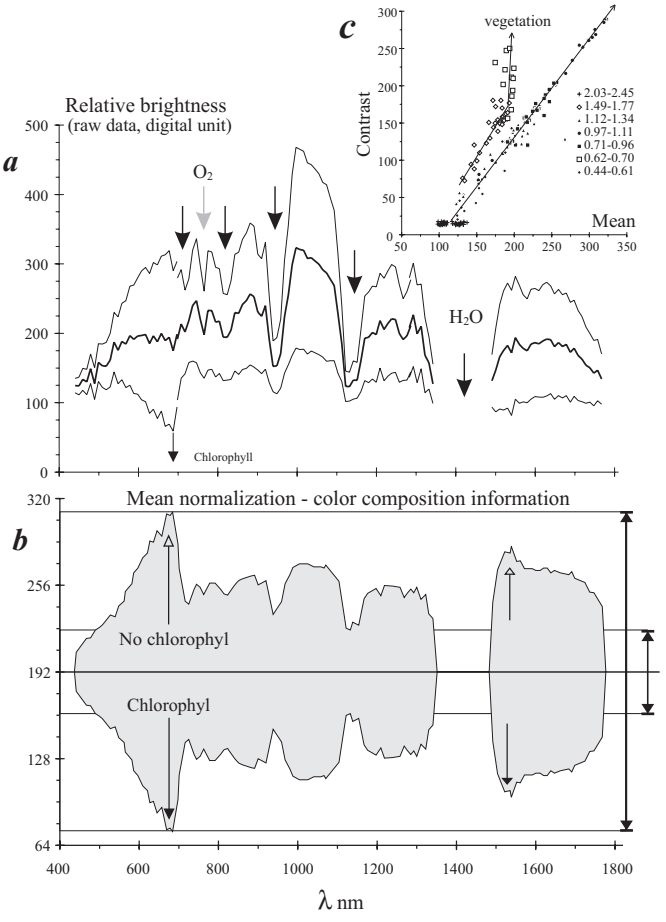

FIG. 2. – Distribution of the information in the AVIRIS image : ***a–*** Raw spectra of the Ronda AVIRIS image; thick line = mean values; thin line = mean +4 and –4 times the standard deviation (4σ). ***b–*** Normalised spectra of the Ronda AVIRIS image (same caption). The grey area is proportional to the amount of information expected in each channel or wavelength. ***c–*** Standard deviation versus mean values for each channel showing the distribution of the information. Two main trends appear according to the contribution of rocks and vegetation

FIG. 2. – *Répartition de l'information de l'image AVIRIS : **a–** Spectre brut de l'image AVIRIS de Ronda; trait épais = valeur moyenne; trait fin = moyenne +4 et –4 fois l'écart-type (4σ). **b–** Spectre normalisé à la moyenne de l'image AVIRIS de Ronda (même légende). La surface grise est proportionnelle à la quantité d'information potentielle pour chaque canal ou longueur d'onde. **c–** Ecart-type fonction de la moyenne pour chaque canal montrant la distribution de l'information. Deux tendances apparaissent en raison des contributions distinctes des roches et de la végétation.*

ternal average relative reflectance" (IAR reflectance) as defined by Kruse [1988]. Data have been compressed for most wavelengths, but stretched in the atmospheric absorption bands. At 700 nm, the over-stretching is due to the chlorophyl absorption. The large percentage (54 %) of pixels completely covered by vegetation shifts the mean value to lower value. Pixels more or less free of vegetation display therefore a strong positive artefact at 700 nm. The same kind of artefact appears at 1 550 nm because of other vegetation features. As already mentioned by Kruse [*In :* Pieters and Englert, 1993] the resulting spectrum fully depends on the average composition grabbed by the whole image. The shape of a spectrum may change from a sub-scene to another. This is not convenient for spectroscopic study and we will rather use calibrations with ground control points for such study.

The plot of standard deviation versus mean value of each channel (fig. 2c) displays various trends. Most of them are aligned on a correlation line except in the range of 620 nm to 700 nm and 1 490 nm to 1 770 nm. These boundaries are used with absorption bands (fig. 2b) to define sub domains which present similar information. As a first exploration of the image, in which we have to explore 150 channels, this sub ranges allow us to make colourful compositions by choosing channels in different sub ranges. At this stage, we are only concerned with information. It is not necessary to identify the real meaning of each channel, we just want to know if there is anything meaningful or not. This may avoid loss of too much time in useless spectroscopic studies. The first one (fig. 1c and 1e) (channel 1530.5 nm in red, 1 253 nm in green and 647.6 nm in blue) shows vegetation in green and ground features in pink to purple. It is remarkable for its violet staining characteristic of serpentine that marks a collapse domain of the southern part of the peridotite, south of a WSW-ENE fault not fully identified on the geological map (fig. 1a). The second one (channel 647.6 nm in red, 746.4 nm in green and 1035.7 nm in blue, fig. 1f) shows that other compositions may display different features. The peridotite is orange in this image and it displays various tones of orange that are scattered differently than the purple ones characteristic of serpentine. This new zoning could be due to the peridotite itself or its weathering. Many other colour compositions can be made with the 150 channels. This is one of the main interests of high resolution "hyperspectral" images that allows many different targets to be highlighted.

Peridotite-vegetation relationships

From a rapid survey of the geological map (fig. 1a) it can be seen that the Ronda peridotite (pale, medium to dark green) is in contact with sedimentary and metamorphic rocks of various compositions and ages. Its boundaries are relatively well defined with smooth curves in the southeastern part and jagged lines in the northwestern part, which is more complicated because of tectonic imbrications [Obata, 1980].

On the AVIRIS colour composite image shown in figure 1c, the Ronda peridotite displays a rather homogeneous light mauve colour partly dashed by greenish zones of various types of vegetation (dark green = pines, intermediate green = bushes and grass, light green = broad-leafed trees). It is very easy to distinguish it from its surrounding rocks, particularly at its southern limits, partially magnified in figure 1-e, and drawn carefully in figure 1c. On the western boundary we can easily characterize the Casares unit (Pzc) made of schist and gneiss completely covered by bush and deciduous forest. On the southern boundary (fig. 1e and 1f), the Oligocene sandstone (To), which is mostly free of vegetation, is well characterized by a washed-out violet colour. The Blanca Unit, on the eastern boundary, displays a more heterogeneous composition. It is made of gneiss (Pzb) very similar to those of the Casares Unit, with a similar green cover, but it also includes marble sheets characterized by a pink staining and a smoother texture (fig. 1e). This unit is in contact with the Casares Unit made of another gneiss (SOm) also completely covered by a vegetation that looks darker (than in Pzb) because of pines. The contact between these units is marked by numerous outcrops of serpentinite (see fig. 1e) that underline the main shallow thrust at the roof of the Ronda peridotite slice. The peridotite itself locally displays strong variations with colours progressively turning to a blue similar to the blue of serpentinite outcrops, particularly in the southeastern part of the massif (fig. 1e). It will be shown below that this colour variation is in good agreement with the serpentine content of peridotites.

The peridotite zonation

If the peridotite is very easy to distinguish from its surrounding units, colour composite images do not allow us to see subtle variations within the peridotite, as they are reported in some geological maps [Lundeen and Obata, 1977, fig. 1a]. This is due to the fact that the petrologic zoning shown on that figure is based on very low compositional variations in the aluminous phases that never exceed 4 % in modal fraction. Our colour composite images also do not allow us to distinguish pyroxene-rich and pyroxene-poor peridotites. This can be surprising when considering that the contribution of pyroxene is usually considered as prominent, even at low concentrations [Adams, 1974 ; Singer, 1981 ; Mustard and Pieters, 1989]. In our case this is likely due to the very heterogeneous distribution of the pyroxene-poor (dunite) and pyroxene-rich (lherzolite) peridotite at the massif scale as seen on figure 1b.

At this time, it is however possible to separate fresh from serpentinized peridotites. The latter are hydrated peridotites that can present various aspects depending on their composition and outcrops conditions [King and Clark, 1989]. In the Ronda peridotite, they can be light green in shear zones or white in extensional fractures forming macroscopic veins. They can be dark when found in little veins, or they can stain olivine in red-brown to yellow when found in a pervasive microscopic net invading the peridotite. Very common in peridotites, the serpentine global amount is often not recorded since it is due to late transformations of olivine, and therefore counted in geological studies as olivine. It is then important to first identify the contribution of this mineral family by field measurements.

SPECTROSCOPY

Field measurement

We use the GER 3700 spectrometer. It analyses light between 300 and 2500 nanometers in three contiguous spec-

tral ranges (or windows) defined by those of a Si CCD and two PbS detectors as shown in figure 3a. For each sample in the field, a white reference Spectralon® is measured. Then, the sample itself is measured and can be compared to the white reference (see fig. 3a). We call DN(i, λ) the count of photons for the sample i and DN(i*, λ) its equivalent for the white reference for each wavelength λ. By using GER factory calibration, each DN spectrum is converted into radiance spectra R(i, λ) and R(i*, λ) (fig. 3b). The reflectance is given for each λ by the ratio :

$$\rho(i,\lambda) = R(i,\lambda) \,/\, R(i^*,\lambda) \qquad (1)$$

For comparison with other spectra, made of n channels between 400 nm and 1800 nm, it is also convenient to calculate the normalised reflectance ρ_n, by dividing each value of a spectrum by the spectrum's mean value :

$$\overline{\rho} = \frac{1}{n} \sum_{\lambda=400}^{1800} \rho(i,\lambda) \qquad (2a)$$

$$\rho_n(i,\lambda) = \rho(i,\lambda) / \overline{\rho} \qquad (2b)$$

740 spectra have been acquired on the Ronda peridotite Massif and a few locations around it. A selection of the most significant spectra are presented in figure 4.

Typical peridotite types are shown in figure 4a. The effectiveness of angle mapping, or its faster calculation with ρ_n, is visualised in figure 4-b with normalised reflectance. The harzburgite, characterised by light brown orthopyroxene, displays an absorption band in the 900-950 nm range. At the opposite, the green clinopyroxenite displays an absorption band in the 1 000-1 050 nm range (and a peak in green). The dunite, with rare pyroxenes, displays a larger band centered at about 1 000 nm closer to the olivine band.

Figure 4c displays lherzolite enriched with white serpentine, mainly lizardite [Cervelle and Maquet, 1982] which is compared with various serpentines of the Ronda Massif. The grey serpentine is a mixture of lizardite with some chrysotile cut by small veins of the same mixture locally enriched in magnetite. It becomes black when it is very rich in magnetite. The green serpentine is a pure chrysotile. Unfortunately, it is impossible to use the OH absorption band at 1 400 nm to better distinguish serpentine in peridotites, as we usually do in laboratory spectroscopy [King and Clark 1989]. The atmosphere completely masks OH bands. It is therefore necessary to look at the overall shape of spectra instead of considering only one absorption band as is shown on spectra extracted from King and Clark [1989] (fig. 4d-2). In normalised reflectance diagrams, the amount of magnetite in serpentines can be underestimated as magnetite rich serpentine is essentially superimposed to magnetite poor serpentine in figure 4d-1. If some weathering effect can increase the global intensity of a spectrum without changing the shape of the spectra, as stated by previous works on the same peridotite [Van der Meer, 1996 ; Chabrillat *et al.*, 2000], one should pay a great attention to many other alterations, for instance serpentinisation, that can dramatically change the spectral shape of any peridotite.

Figure 4e is a compilation of other local rocks. The gabbro, found inside the peridotite, contains brown pyroxenes. Two samples of migmatite are presented, one is rich in plagioclase the other in biotite. Two gneisses are also presented, dark because of biotite (and a few garnets), or light

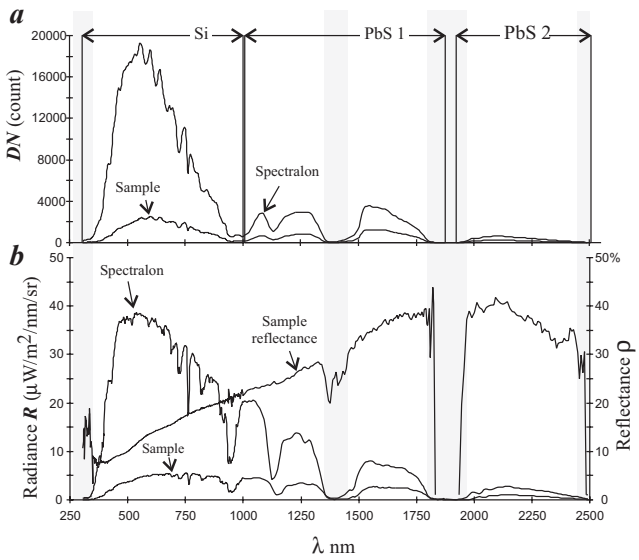

FIG. 3. – GER 3700 data acquisition : ***a***– Raw spectrum in device unit (DN) with wavelength range of the three detectors used in the spectrometer. At each station, a white plate (Spectralon®) is analyzed prior to any sample measurement. ***b***– Calibrated spectra as given by GER 3700 using factory calibrations. The reflectance is the ratio, at each wavelength, of the sample intensity divided by the white reference (Spectralon®) intensity.

FIG. 3. – *Acquisition des données GER 3700 :* ***a***– *Spectre brut en unité capteur (DN) et domaine de sensibilité des trois capteurs du spectromètre en longueur d'onde. Pour chaque station de mesure, une plaque blanche de référence faite de Spectralon® est analysée avant toute mesure d'échantillon.* ***b***– *Spectre calibré tel qu'il est donné par GER 3700 grâce à son calibrage en usine. La réflectance est le rapport, pour chaque longueur d'onde, entre l'intensité lumineuse mesurée sur l'échantillon et celle qui est mesurée sur la référence blanche (Spectralon®).*

because high content in plagioclase. All these rocks display strong variations in their spectrum's intensity. This is not the case in figure 4f with the presentation of their normalised reflectance ρ_n. The garnet, characterized by a peak (arrow in fig. 4f) in the red band is particularly difficult to catch. The feldspar-rich gneiss is almost identical to the feldspar-rich migmatite which itself appears very different from the biotite-rich migmatite. All these rocks are therefore very difficult to separate from one another and therefore difficult to map, at least in the 400 to 1800 nm wavelength interval. The gabbro, made of pyroxene and plagioclase also presents a good correlation with some peridotite types (compare fig. 4f with fig. 4d). Knowing that it contains at least 20 times more plagioclase than any Ronda lherzolite, we can believe that detection of those plagioclases is impossible in any Ronda lherzolite. On the contrary, the similarity between serpentine (fig. 4d) and rocks enriched in plagioclase (fig. 4f) leads to believe that some serpentinized peridotites may display a good correlation with plagioclase-rich rocks. It is therefore impossible to detect 1 to 4 % of plagioclase in the Ronda peridotite in the range 400-1800 nm. This can be seen also when comparing plagioclase spectra from Hiroi and Pieter [1994] with serpentines spectra from King and Clark [1989] in the same window between 400 nm and 1800 nm.

Figure 4g displays various soils and sands covering the peridotite. They mostly present spectra similar to those of peridotite but with the main absorption band shifted toward

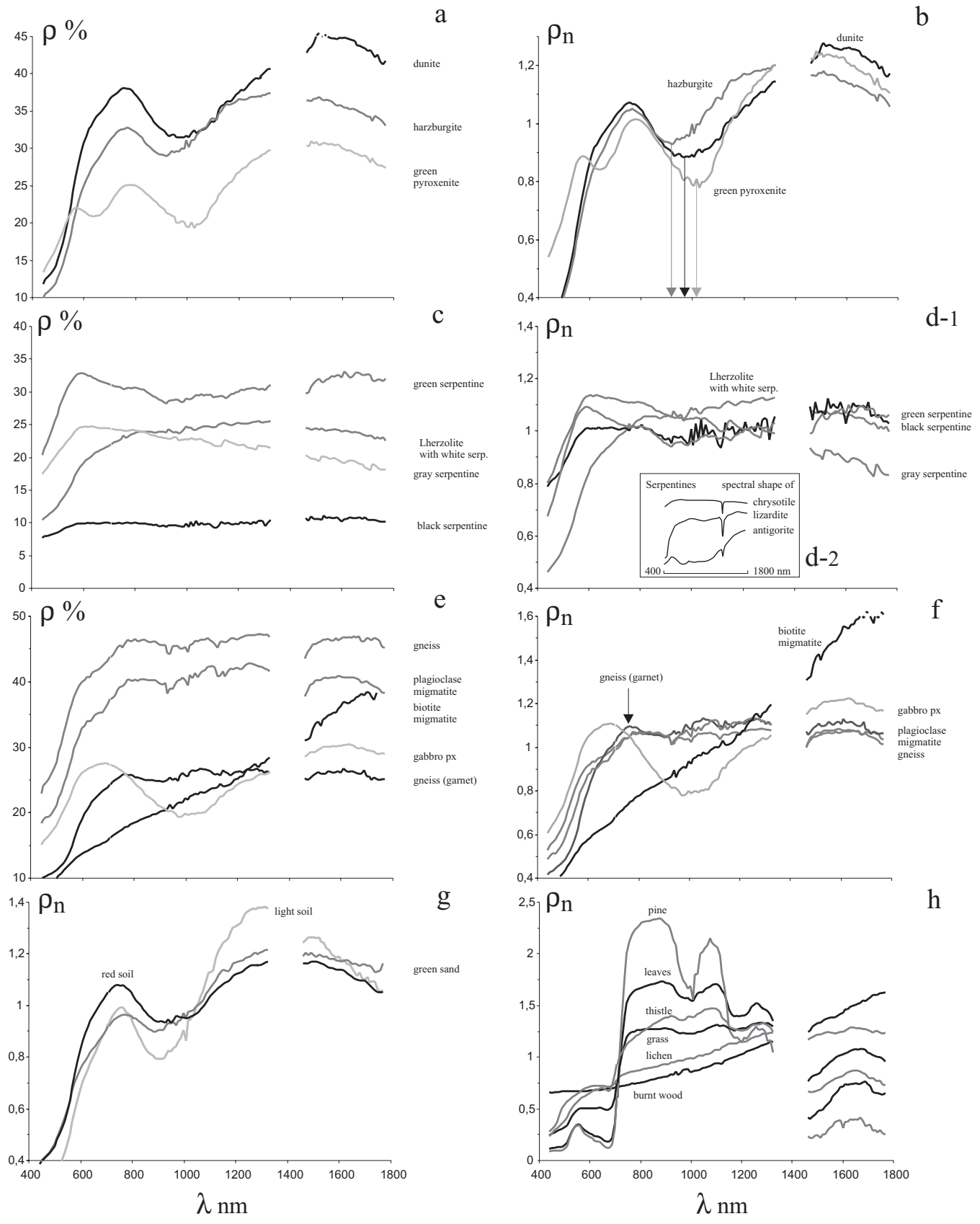

FIG. 4. – Field measurements. Reflectances ρ of various samples in a, c and e and their corresponding normalised reflectances ρn in b, d and f. g ρ_n of various soils. h spectra of a few vegetation types found on and around the peridotite. See text for discussion.

FIG. 4. – *Collection de mesures de terrains. Réflectance* ρ *de différents échantillons en* **a**, **c** *et* **e** *et leur spectre de réflectance normalisée* ρ_n *en* **b**, **d** *et* **f**. *Présentation de quelques spectres de sols en* **g** *et de végétation typique de la péridotite en* **h**. *Voir texte pour discussion.*

900 nm (the most obvious one is the green sand of clinopyroxene that match the harzburgite).

Figure 4h is a collection of vegetation samples, including burnt wood. All spectra are normalised reflectance (eq. 2b). This makes it easier to separate broad-leafed trees, conifers, thistles, grasses, lichens and burnt woods. They all present different patterns which should give contrasted angle mapping values. In the grass removal algorithm presented below to enlarge the area of peridotite mapping, we only consider the grass covering the outcrops. It can be seen in figure 4h that a low percentage of plants other than grass can modify the reflectance spectrum. Removing grass instead of thistle induces a tilt of the resulting spectrum. It is therefore necessary to better define the contribution of the vegetation when one is mapping subtle variations of the mineralogy. This is not often done in applications of remote sensing to geological studies.

The normalisation is convenient when working in sharp topography, where light intensity reflected by outcrops can vary a lot with slope orientations (fig. 1h) and with the shadowing factor which is a function of the slope roughness [Despan *et al*., 1998]. This is however a problem when one wants to look at mineral variations. It is clear from the comparison of figure 4a, 4c and 4d with fig. 4b, 4d and 4f respectively, that the intensity information could have been very useful to estimate small variations of the mineralogy. However this implies to develop full bidirectional reflectance studies like Despan *et al.* [1998] and to have access to a very precise digital elevation model.

Image calibration

Like many authors [e.g. Chabrillat, 1995] we use the classical empiric line correction [Roberts *et al.*, 1986 ; Kruse *et al.*, 1990 ; Richards, 1994 ; Farrand *et al.*, 1994]. This process requires black and white control points. The black one fixes the offset and its difference to the white one fixes the signal amplitude or gain (fig. 5). Best ground control points are determined on colour composite images by displaying the minimum, mean and maximum values of each spectrum on red, green and blue channels respectively (fig. 1d). The vegetation is blue and rocks are orange. Pixels best suited for correction are standard black (black control point) and standard white (white control point) pixels because of the flatness of their spectrum. The white control point found at location xw=15 and yw=63 (image coordinates) is probably due to a specular reflection of the sun light. The black control point located at xb=0 and yb=174 resembles biotite-rich migmatite in the field (R(b,λ), fig. 5b). It is important to point out that both control points (DN(xw,yw,λ) ; DN(xb,yb,λ)) are located at the same altitude. For any channel λ between 400 and 1800 nm, the calibration of the radiance of a pixel (R(x,y,λ) in $\mu W/m^2/sr/nm$) involves the determination of the gain C(λ) which is equal to the ratio of the difference between the radiance of the spectralon R(b*, λ) and that of the field black reference (R(b,λ)) measured at the same time, to the difference between the digit number of the white pixel DN(xw,yw,λ) and the digit number of the black pixel DN(xb,yb,λ) :

$$C(\lambda) = \frac{R(b^*, \lambda) - R(b, \lambda)}{DN(xw, yw, \lambda) - DN(xb, yb, \lambda)} \qquad (3)$$

The empiric line correction is effectively given by :

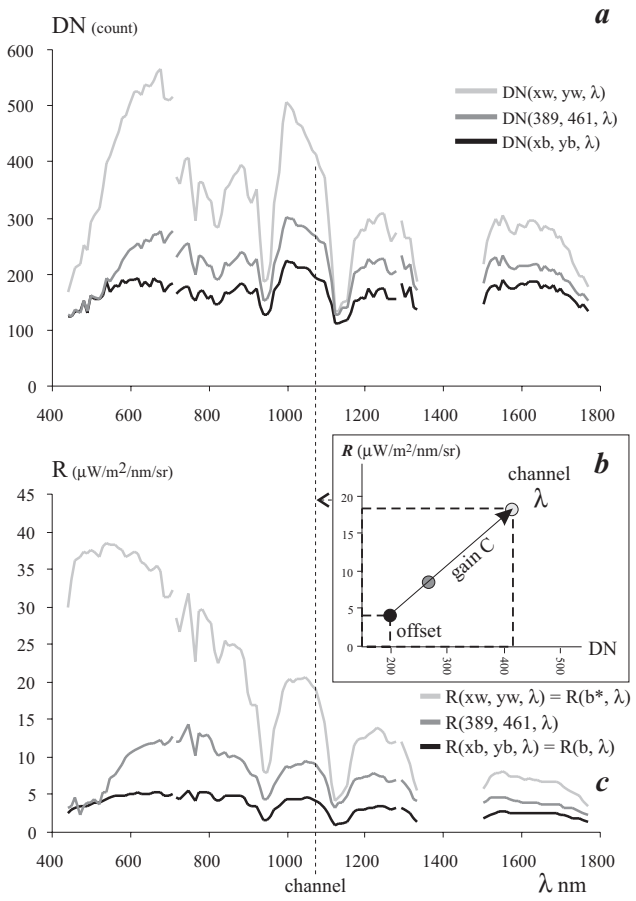

FIG. 5. – Empiric line correction applied to AVIRIS data from Ronda (1992 data limited at 1800 nm). ***a***– Raw intensity (digital number DN) of the AVIRIS image with control point at location xw=15, yw=63 for the white reference and xb=0, yb=174 for the black reference (x=389, y=461 is an example of peridotite spectrum); ***b***– Gain and offset diagram showing the procedure of calibration; ***c***– Result of the calibration for the 3 pixels presented in *a*. The white and black references are given by a field measurement of a Spectralon® (R(b*,λ)) and of a sample of a biotite-rich migmatite (R(b,λ)).

FIG. 5. – *Ajustement linéaire empirique ("empric line correction") des spectres de radiance de l'image AVIRIS de Ronda (donnée de 1992 bornées à 1800 nm).* ***a***– *Intensité brute (digital number DN) de l'image AVIRIS avec points de contrôle en xw=15, yw=63 pour la référence blanche et xb=0, yb=174 pour la référence noire (x=389, y=461 est un exemple indépendant de spectre de péridotite).* ***b***– *Diagramme gain et offset illustrant la procédure de calibrage;* ***c***– *Résultat du calibrage pour les trois pixels présentés en a. Les références blanche et noire sont données par des mesure de terrain d'un Spectralon® (R(b*,λ)) et un échantillon de migmatite riche en biotite (R(b,λ)).*

$$R(x,y,\lambda) = R(b,\lambda) + (DN(x,y,\lambda) - DN(xb,yb,\lambda))\cdot C(\lambda) \qquad (4)$$

and illustrated in figure 5a. One can note that R(xw,yw,λ) = R(b*,λ). It is important to note here that the calibration of a hyperspectral image can be done six years after its acquisition. One limitation of this correction is the lack of information on the atmosphere effect in an area with large variations of elevation. In order to overcome this difficulty, an empirical atmospheric correction is carried out similarly to the study of Roberts *et al.* [1997].

The reflectance (ρ(x,y, l)) can then be calculated over the full image by :

$$\rho(x,y,\lambda) = R(x,y,\lambda) / R(xw,yw,\lambda) \qquad (5)$$

but should not be confused with the relative brightness (r(x,y, λ)) defined by :

$$r(x,y,\lambda) = DN(x,y,\lambda) / DN(xw,yw,\lambda) \quad (6)$$

Atmospher thickness

The information about the atmosphere thickness, which is proportional to elevation, can be estimated by using the index I_e which describes the depth of the water vapour absorption band at 948 nm (fig. 5c) :

$$I_e(x,y) = 2\ \rho(x,y,948) / (\rho\ (x,y,920) + \rho\ (x,y,968)) \quad (7)$$

This information can also be readily observed in a greyscale image of channel 948 nm (fig. 6-a). Pixels at the Los Reales Peak are brighter than pixels at its bottom. The index I_e is similar to the index of Bibring *et al.* [1991], but one can also use the narrow/wide band ratio of Carrère and Conel [1993]. It is the ratio of two averages, between 935 nm and 955 nm (for narrow) and between 920 nm and 970 nm (for wide). We want to emphasise that the use of relative brightness may induce misinterpretation since the offset is not taken into account. This is particularly well illustrated by the comparison between estimation of the atmospheric thickness based on r and ρ in figure 6b and 6d. The forest fire area (black in fig. 6a), appears white on the I_{er} map in figure 6c ($I_{er}(x,y) = 2\ r(x,y,948) / (r(x,y,920) + r(x,y,968))$), whereas it is grey as expected on the I_e map in figure 6f. The opposite effect is obtained in areas of high relative brightness (broad-leafed trees, sand stone and marble) which appear much too dark in figure 6c. This problem occurs for any absorption feature and reminds to those who are familiar with band ratio studies (classical in remote sensing textbooks) that the atmosphere should never be neglected.

From figure 6f, a digital elevation model (DEM) can be produced by using a linear regression between control points of the Ie map and a topographic map like $H(x,y) = a.(Ie(x,y) - b)$. However, H(x,y) is also biased by a regular noise due to the poor quality of the data in the absorption band (see fig. 2a). This noise can be partially removed by a low-pass filter, but a few linear artefacts remain. A shadow calculation, given by ER Mapper, highlight this effect (fig. 6g). It can be isolated in the power spectrum of the Forward Fast Fourier Transformation (FFFT, ER Mapper) of the I_e map image as a small patch (arrow, fig. 6-h). The meaningful signal is identified by a white ellipse in figure 6h. During a backward transformation (BFFT, ER Mapper), undesired components, outside of the white ellipse, are smoothed out and the image is rebuilt without blank noise and linear artefact. The shadow calculation is now more effective (see fig. 6i). However, if the altitude can be closely estimated (compare fig. 6j and 6k) by using an ultimate correction along the y direction (there is a tilt of 150 m between the SE and the NW ends of the I_e map), it doesn't have enough resolution for accurate slope calculations. The topography remains wavy at the scale of a few pixels and lighting corrections cannot be done. The topography of figure 6j is presented here to show that atmosphere was correctly estimated on the basis of its calibration with field measurements six years after the image acquisition.

Atmosphere removal

The full correction of the atmosphere effect, particularly in the water vapour absorption band (see spectra of fig. 6d), usually requires a model for the atmosphere [Gao *et al.*, 1993 ; Farrand *et al.*, 1994 ; Roberts *et al.*, 1997]. In fact it can be directly estimated with a collection of Spectralon® measurements.

The shape of the atmosphere function (AF, fig. 7a) is the ratio of a Spectralon measured at 1 400 m and a Spectralon measured at 350 m. A new index I_c is defined (fig. 7c). If I_e is proportional to the atmosphere thickness, I_c is proportional to the atmosphere density which increases when going down the valley. Of course, since many factors, including weather conditions and sun elevation [Roberts *et al.*, 1997], can modify a spectrum of Spectralon®, its measurement at both altitudes must be performed in the shortest time interval. This was done in July 1997 in two sites around noon, less than two hours apart, but six years after the AVIRIS acquisition in 1991. Five spectra were acquired, in less than 20 minutes, on each site AD around 1 400 m and AG around 350 m, at the top and at the bottom of Los Reales mountain (see fig. 1c). The atmospheric function AF is given by :

$$AF(\lambda) = \frac{R(siteAG^*,\lambda)}{R(siteAD^*,\lambda)} - 1 \quad (8)$$

It is 0 outside the absorption features as it can be seen in figure 7a between 350 and 1 800 nm. The same kind of ratio was used by Gao *et al.* [1993] to estimate the sensitivity of their analysis to the water vapour column of the atmosphere. The atmospheric absorption bands can then be removed without any other knowledge of the exact composition of the atmosphere and the reflectance ρ_a is obtained by :

$$\rho_a(x,y,\lambda) = \rho\ (x,y,\lambda) \cdot \{1 + (AF(\lambda) \cdot I_c(x,y))\} \quad (9)$$

where $I_c(x,y)$ is a correcting factor proportional to $I_e(x,y)$-1. It is equal to 0 at 350 m, greater than 0 over 350 m and smaller than 0 under 350 m. For a selection of pixels at various altitudes, we manually select a first estimate of I_c that removes the water vapour absorption artefact and plot its value versus I_e (fig. 7c). The best fitting polynomial function linking all couples (I_e, I_c) presented below can then be used in equation 9 to automatically correct all the pixels of the image :

$$I_c(x,y) = 0.1588 \cdot (I_e(x,y)\text{-}1)^4 + 6.7184 \cdot (I_e(x,y)\text{-}1)^3 - 11.035 \cdot (I_e(x,y)\text{-}1)^2 + 9.3197 \cdot (I_e(x,y)\text{-}1) - 0.0159 \quad (10)$$

A test on 250 pixels is used to adjust the coefficient of the function. The index Ie-1 calculated on the resulting spectra ($(Ie\text{-}1)_2$ in fig. 7c) is always close to 0 ($\sigma = 0.001$) which confirms that the atmosphere absorption band has been fully removed (fig. 7d). The black ground control point used for the empirical line correction is not only made of biotite rich migmatite, but probably includes a shade component. There is negative reflectance (fig. 7d) so all spectra have to be shifted and tilted upward towards the long wavelength. This can be done with equation 11 with proper coefficients in $s(\lambda)$:

$$\rho_c(x,y,\lambda) = \rho_a(x,y,\lambda) - s(\lambda) \quad (11)$$

In the following text we will note ρ without a c index since all data are fully calibrated. It is difficult to compare AVIRIS and GER 3700 data (fig. 7e) without sufficient

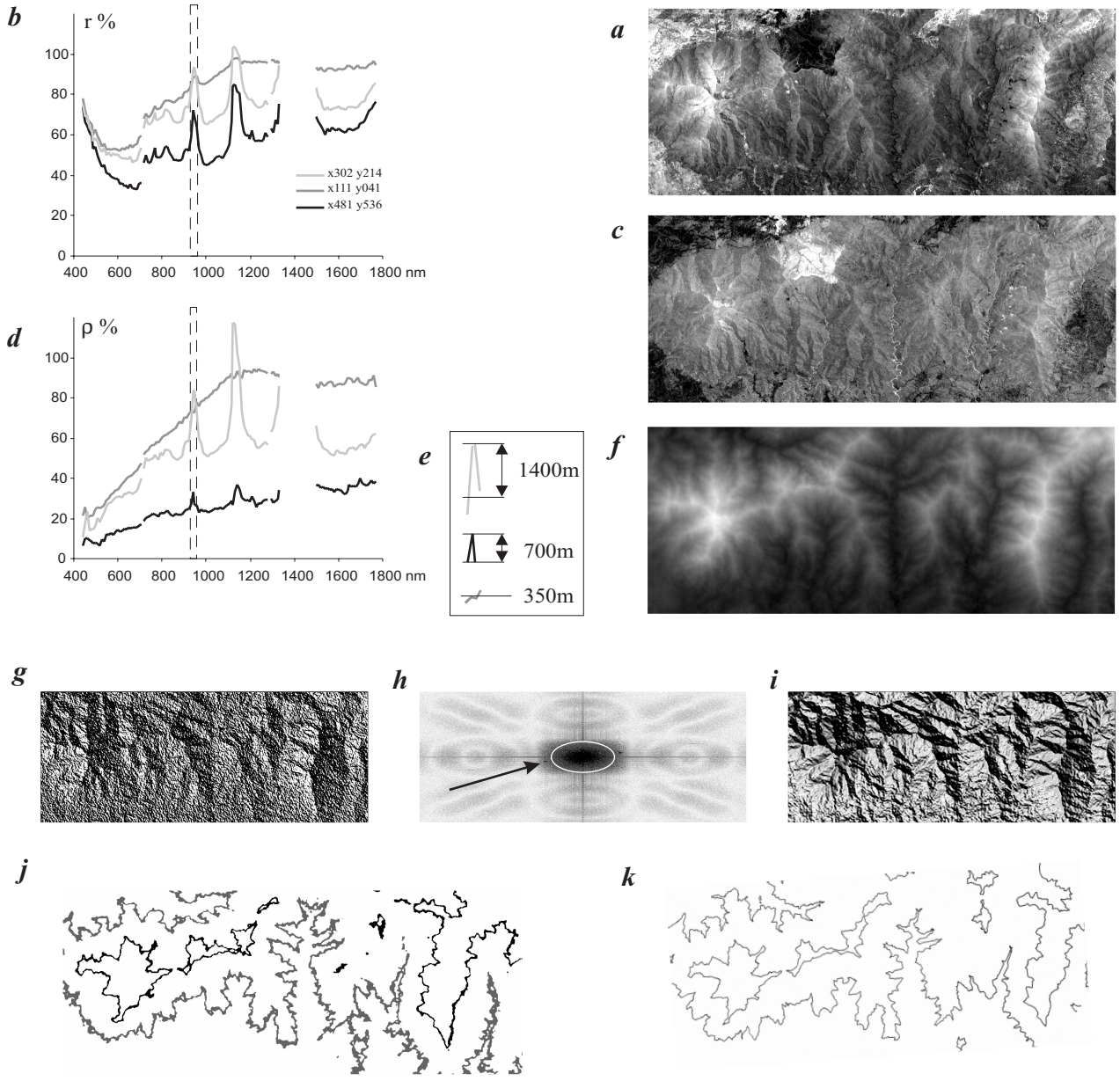

FIG. 6. – Atmosphere thickness. ***a***– Greyscale image of channel 940 nm showing the effect of the water vapour absorption band. As it decreases with increasing altitude, pixels at the top of Los Reales mountain looks brighter than pixels at its bottom. ***b***– The calculation of the reflectance from a unique reference at 350 m (with a dip well at 940 nm) leads to the formation of artefacts in each absorption band of the atmosphere. ***c***– The height of this artefact can be measured by the ratio between the intensity at 948 nm (well of the water vapour band) and the intensities at 920 nm and 968 nm (shoulders of the water vapour band) and presented in a greyscale image. ***d***– The height of this artefact is effectively linked to the altitude when spectra are fully calibrated as it is shown in ***e***. ***f***– The resulting map of atmosphere thickness (which explains the water vapour absorption) can then be presented as a digital elevation model. ***h***– The amount of noise is visualised by a shadow calculation. ***g***– This noise is partly removed by a combination of a Gaussian filter on the image and on its Fourier transform (Er Mapper FFT and lowpass filters). ***i***– Same as g with filtering. ***j***– Selection of pixels at 500 m (grey) and 1 000 m (black). ***k***– Same altitudes obtained from a topographic map.

FIG. 6. – *Epaisseur de l'atmosphère.* ***a– N****iveaux de gris du canal 940 nm montrant les effets de la bande d'absorption de la vapeur d'eau. Comme celui-ci décroît avec l'altitude, les pixels au sommet du mont Los Reales sont plus clairs que ceux du pied de ce mont.* ***b–*** *Le calcul de la réflectance à partir d'une unique référence à 350 m (avec une profonde bande d'absorption à 940 nm) entraîne la formation d'artéfact au niveau de chaque bande d'absorption de l'atmosphère.* ***c–*** *La hauteur de cet artefact peut être mesurée par un rapport entre l'intensité à 948 nm (au fond de la bande d'absorption de la vapeur d'eau) et l'intensité à 920 nm et 968 nm (les plateaux de part et d'autre de la bande d'absorption de la vapeur d'eau) et représentée en niveaux de gris sur une image.* ***d–*** *la hauteur de cet artefact est effectivement liée à l'altitude lorsque les spectres de radiance sont bien calibrés comme indiqué en* ***e****.* ***f–*** *La carte de l'épaisseur calculée de l'atmosphère (qui explique l'absorption de la vapeur d'eau) peut alors être représentée comme un modèle numérique de terrain.* ***h–*** *La quantité de bruit est bien visualisable par la projection des ombres sur ce modèle numérique de terrain.* ***g–*** *Ce bruit est en partie retiré grâce à une combinaison de filtre gaussien de l'image et de sa transformé de Fourier (Er Mapper FFT et filtre passe-bas).* ***i–*** *Identique à g après filtrage.* ***j–*** *Sélection de pixel à 500 m (gris) et 1000 m (noir).* ***k–*** *Courbes de niveau à 500 et 1 000 m extraits de la carte topographique.*

knowledge of topography and sample roughness. We will then use the normalised ρ_n as defined in equation 2 but with full calibration of ρ (ρ_c). This calculation of ρ_n should not be confused with the IAR (internal averaging relative) reflectance which is normalised to the average spectrum of the whole image whereas ρ_n is normalised to its own aver-

age value, which may be different from one pixel to the next one. Figure 7f displays normalised reflectance showing a very good agreement between AVIRIS and GER 3700 data.

New AVIRIS data benefits from on-board calibration. However such calibration must be complemented with the kind of analysis developed in the present study since local atmospheric effect cannot be fully removed. Therefore, field measurements are necessary. A calibration can be achieved without any other data (atmospheric data) than field measurements, even 6 years later, and the field measurements are necessary to remove atmospheric artefacts on reflectance spectra.

Grass removal

Most of the outcrops measured in the field are made of a patchwork of homogeneous areas of vegetation and rocks. One 20 ×20 m pixel is made of 20 ×20 cm sub-pixels of pure vegetation or pure rock as shown in figure 1g. Without considering spectral interaction between sub-pixels, one pixel can therefore be seen as an addition of V % sub-pixels of grass and 1-V % sub-pixels of rock (fig. 8c) :

$$\rho(x,y,\lambda) = V\ \rho(\text{grass},\ \lambda) + (1\text{-}V)\ \rho_v(x,y,\ \lambda) \quad (12)$$

where $\rho(\text{grass},\ \lambda)$ is the reflectance spectrum of grass and $\rho_v(x,y,\ \lambda)$ is a spectrum which contains the geological information. As discussed by Elvidge *et al.* [1993], the grass cover can be estimated by using the following vegetation index I_v (see also fig. 9-a) :

$$I_v(x,y) = \frac{(\rho_n(x,y,598)\cdot\rho_n(x,y,746))}{(\rho_n(x,y,667)\cdot\rho_n(x,y,677))} \quad (13a)$$

The relation between grass cover percentage V and this index I_v is given by the best fitting curve (fig. 9b) :

$$V(x,y) = 0{,}1906\ (\ I_v(x,y)^3 - 1.3311\ \cdot\ I_v(x,y)^2 + 3.4421\ \cdot\ I_v(x,y) - 2.2603 \quad (13b)$$

It is then possible to remove the grass contribution by using a correction similar to the atmosphere correction. Since we consider neither the slope, nor the lighting angle, the first order mixing equation 12 cannot be used and an empirical expression has been determined to infer the geological information from the spectrum :

$$\rho_v(x,y,\lambda) = \rho(x,y,\lambda)\cdot(1 + (1/\rho_n(\text{grass},\ \lambda) - 1)\cdot V(x,y)) \quad (14)$$

where $\rho_n(\text{grass},\lambda)$ is a normalised spectrum of grass (fig. 8a). If the vegetation coverage is larger than 50 %, the noise of the resulting data becomes as large as the geological signal.

Figure 8c and 8e display applications to AVIRIS data for harzburgite and serpentine. The results are shown in figure 8d and 8f respectively. The grass removal correction presented here does not alter the information about the peridotite when the proper vegetation is removed, and the noise remain stable. However, outcrops are not always covered by only one kind of grass (fig. 1i), and we can expect a better removal of the vegetation by using more complex models of vegetation coverage including grass, thistle, and many other plants, by using more sophisticated models of vegetation [Jacquemoud, 1993]. This is particularly important when using angle mapping techniques, as we will show below.

Normalised reflectance distances

Like Van der Meer [1996] we look at the correlation coefficient between field and airborne measurements. We use the following spectral angle mapping (SAM) defined by Kruse *et al.* [1993] to compare each pixel (x,y) with a sample j :

$$\text{angle}\ (x,y,j) = \cos^{-1}\left(\frac{\sum_\lambda \rho(x,y,\lambda)\cdot\rho(j,\lambda)}{\sqrt{\sum_\lambda \rho(x,y,\lambda)^2}\cdot\sqrt{\sum_\lambda \rho(j,\lambda)^2}}\right) \quad (15)$$

and to built the channel j of an image of angle mapping with :

$$I_a(x,y,j) = 1000\ /\ \text{Angle}(x,y,j) \quad (16)$$

with I_a being a short integer more suitable to code images (2 bytes / pixel).

The angle is null and I_a intensity is maximum when field measurements and airborne data match perfectly. I_a is not sensitive to slope angle and variations of intensity [Kruse *et al*., 1993]. The same calculation using ρ_n instead of ρ gives exactly the same result, it only compares shape of spectra. When ρ_n is available, one can substitute the usual equation 15 by the following equation 17 which gives a similar result but is faster to calculate on a personal computer :

$$D(x,y,j) = \frac{1}{n}\sum_\lambda \frac{\rho_n(x,y,\lambda) - \rho_n(j,\lambda)}{\rho_n(x,y,\lambda)} \quad (17)$$

with the corresponding image given by I_d (short integer) :

$$I_d(x,y,j) = 1000/D(x,y,j) \quad (18)$$

Both calculations were applied to various sites with comparison to harzburgite in figure 9a to 9f. The angle found with ρ and ρ_n is identical (compare figure 9a with figure 9b, 9c and 9d). D is always very close to the angle written in radian and the value of all indexes I_a and I_d are close enough to produce almost identical images. We thus display only Id maps (fig. 9f) with a greyscale (fig. 9e) increasing from white for low intensity to black for high intensity. The darkest pixels of figure 9f are therefore rich in harzburgite. D is also very useful to visualise the process of calculation. It is the mean distance D between the two reflectance spectra at each wavelength in the interval 400-1800 nm (see double arrows in fig. 9b, 9c and 9d).

Neither angle mapping nor distance mapping, takes into account real intensities. A flat spectrum, with low mean intensity, will have exactly the same angle or distance D to a black reference than a light one with high intensity. The SAM technique analyses only the shapes of the reflectance spectra and cannot distinguish between spectra similar in shape but of significantly different intensities. So, if it is effectively sensitive to the lighting intensity, it misses an important information which is generally useful. To do so, one would have to take into account the topography as mentioned at the end of § Field measurement.

In the colour composite images of Id maps (fig. 10a-b-d-e-g-i) the greyscale of each red, green and blue channel is positive (from black to white) and each channel uses a specific scale to display 99 % of the pixel in a range between black and red, green or blue respectively (see scale minimum and maximum values in figure 10g and 10i captions). The most significant pixels are therefore light

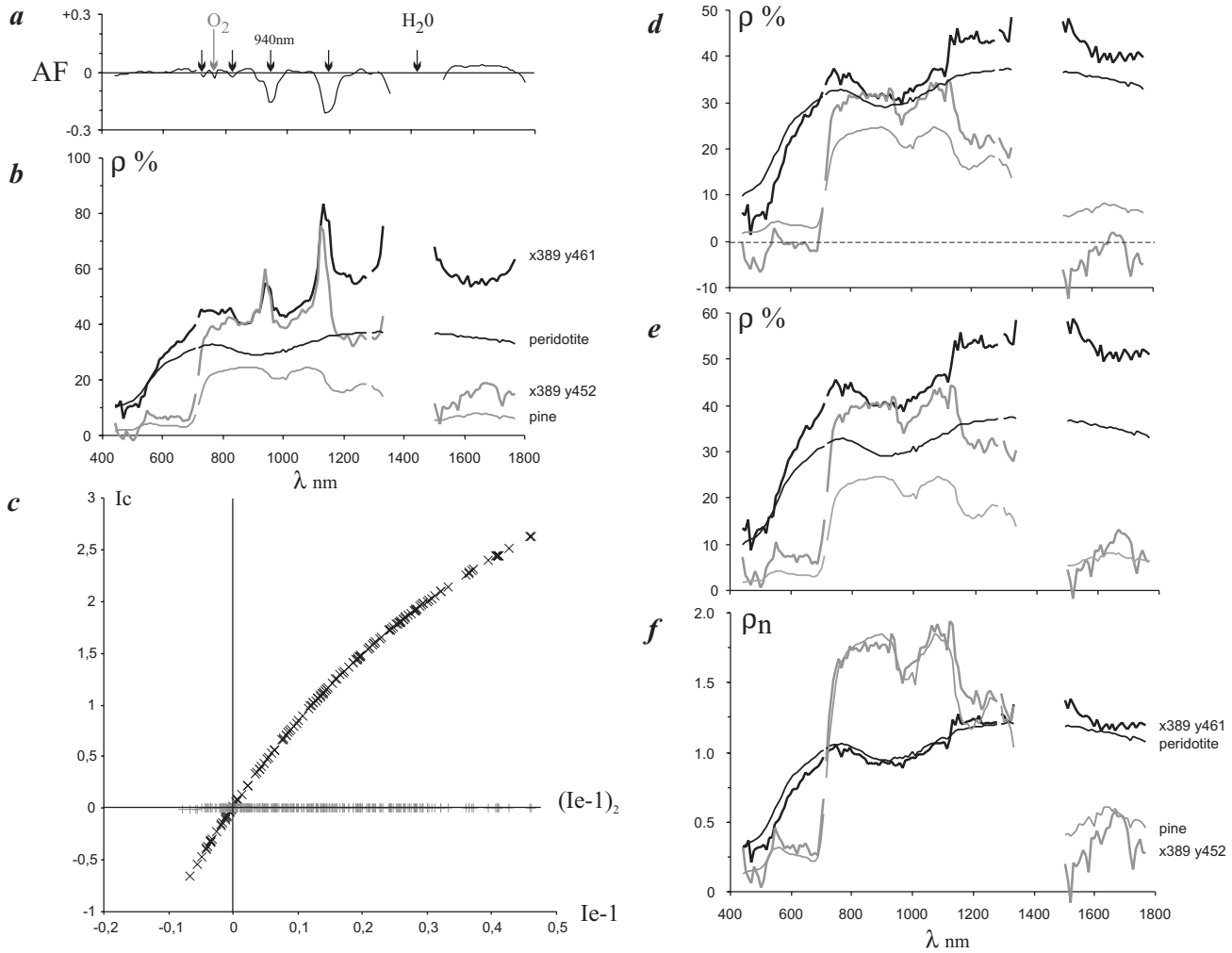

FIG. 7. – Atmosphere removal. ***a***– The atmosphere function (AF) is the ratio between the radiance of one Spectralon® plate analysed at 350 m and the same plate analysed at 1400 m; ***b***– Comparison of calibrated spectra (at various xy pixel locations) with field measurement (pine and peridotite); ***c***– plot of index I_c versus $(I_e\text{-}1)$ and $(I_e\text{-}1)_2$ versus $(I_e\text{-}1)$ (see text for detail); ***d***– Resulting spectra without atmospheric absorption features ; ***e***– Adjustment to zero; ***f***– Normalised reflectance ρn showing the good correlation between AVIRIS data and field measurements.

FIG. 7. – *Correction atmosphérique.* ***a***– *La fonction représentant la contribution de l'atmosphère (AF) est donnée par le rapport de radiances de Spectralon® mesuré à 350 m et à 1 400 m ;* ***b***– *Comparaison entre spectre calibrés (pour différents site de coordonnées pixel xy) avec des mesures de terrain (pins et péridotite);* ***c***– *Dessin de l'indice I_c en fonction de $(I_e\text{-}1)$ et $(I_e\text{-}1)_2$ en fonction de $(I_e\text{-}1)$ (voir texte pour détails).* ***d***– *Spectres résultants sans bande d'abosorption de l'atmosphère;* ***e***– *Ajustement à zéro ;* ***f***– *Normalisation de la réflectance* ρn *montrant la bonne corrélation entre les données AVIRIS et les mesures de terrain.*

and well coloured whereas less significant pixels are dark. In figure 10g and 10i, pixels with strong vegetation index are set to white to visually enhance pixels characteristic of rocks or soils.

Spectral angle mapping : application to the vegetation of the Ronda massif

The colour composite image made of oaks, young pines and old pines I_d maps in red, green and blue channel respectively (fig. 10a) display the broad-leave forest in yellow where oaks are dominant. Bush areas are violet, and conifer (dominant) forests are green. The spectral distance to 3 samples of oaks and pines can therefore be used to map other trees. In this colour composition (fig. 10a) areas free of forest appear black. The colour composite image of I_d maps of thistle, long grass and lavender (in red, green and blue channels respectively, fig. 10b) also maps other plants as it can be seen by the blue colour of all forest where lavender is obviously not common. Thistle, or any plant having a similar spectra, appears red in the southern part of the massif, covering the northern part of the serpentinized peridotite area presented in figure 1e. This surprising correlation between a serpentine and a thistle area could not be seen in the field in 1997 because of a recent forest fire. On the contrary, we were able to confirm in the field (fig. 1g to 1i) that plants and grass which appear green in figure10b are effectively abundant all over the peridotite.

The index of vegetation I_v (equation 12) used to calculate grass removal function (equation 14) is shown in figure 10c. The area apparently free of vegetation is dark blue (false colour scale), grassland appears cyan to green whereas bushes and forests are yellow to red. The algorithm is illustrated in figure 10d and 10e. It is only applied to pixels with I_v values lower than 0.5 (blue to green in fig. 10c). The red, green and blue channels of figure 10d are peridotite (harzburgite), grass and thistle Id maps calculated on the original image of reflectance ρ. The same index (Id) has been calculated after grass removal in figure 10e (ρ_v).

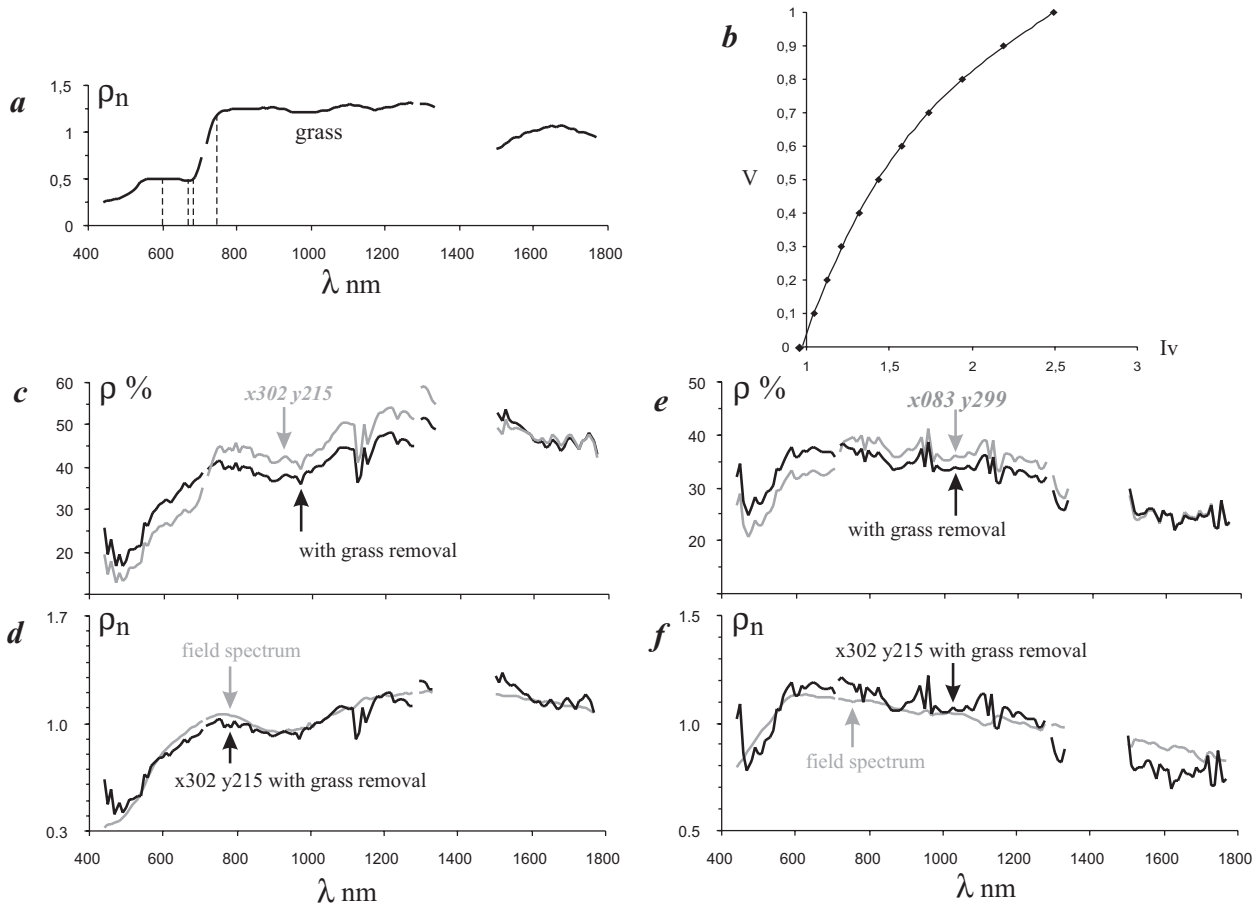

FIG. 8. – Grass removal. ***a***– Normalised reflectance of grass; ***b***– Diagram of vegetation cover versus index of vegetation I_v (see text for discussion). ***c***– Reflectance of harzburgite with 40.6 % grass cover and its spectra after grass removal. ***d***– Comparison of the same spectra with field measurements. ***e*** and ***f***– Same processing with grey serpentine covered by 26.4 % grass.

FIG. 8. – *Retrait de l'herbe.* ***a****– Réflectance normalisée de l'herbe;* ***b****– Diagramme de la couverture de la végétation en fonction de l'indice de végétation* I_v *(voir texte pour discussion).* ***c****– Réflectance de l'harzburgite avec 40,6 % de couverture par de l'herbe et son spectre après retrait de l'herbe.* ***d****– Comparaison du même spectre avec une mesure de terrain.* ***e*** *et* ***f****– Même traitement avec une serpentine grise recouverte par 26,4 % d'herbe.*

The extension of the peridotite is a lot larger in the second image (fig. 10e). Most of the green areas of grass have been replaced by red areas indicating a better correlation with any lherzolite except in the forest fire area which becomes brown. The strong index I_d of peridotite in the burnt area of figure 10d is in fact amplified by the overall flat pattern of the spectrum. As mentioned before, angle mapping effectively works with normalised reflectances. When a spectrum is low in intensity and flat its relative shape can change dramatically with little variations of intensity with wavelength. The limestone Jn (see location in fig. 1a) presents the same kind of amplification because of its white and flat spectrum between 400 nm and 1 800 nm.

Spectral angle mapping : application to the rock type of the Ronda massif

The colour composite image of figure 10g is made of harzburgite (fig. 9f), cpx-rich pyroxenite (fig. 9g) and lherzolite with white serpentine (fig. 9h) Id maps. The blue channel is identical in figure 10i but the red channel is an Id map of grey serpentine (lizardite with little magnetite, fig. 9i) and the green channel is an Id map of green serpentine (chrysotile, fig 9j).

As expected, since olivine is the most important component of any peridotite type, both lherzolites (fig. 9f and 9h) display stronger I_d intensity than pyroxenite (fig. 9g). However, the variation of intensity found between peridotite types do not match the geological boundary presented in figure 1a or 1b. On figure 10g the peridotite is orange to yellow with increasing absorption feature around 900 nm and becomes green when relatively enriched in pyroxene along fresh cuts, such as the northern road. However, the green patch south of Los Reales mountain is not particularly rich in pyroxene (neither in cpx). On the contrary, the white lizardite is well mapped over the peridotite by its blue to cyan colour in figure 10g.

Surprisingly, it is more difficult to map this lizardite (fig. 9i) with a sample of serpentine in which the lizardite is clearly the main component. The chrysotile also presents low Id intensities over the peridotite (fig. 9j) but it seems more evenly scattered than the lizardite which occupies narrower areas (arrows in fig. 9i). The better site for lizardite is well highlighted in the figure 10i with a red colour which is exactly the area of thistle-like plants presented in figure 10b.

Both serpentines are characterised by strong I_d intensities along roads and streams. In fact, peridotites often break down along faults where serpentines are usually abundant.

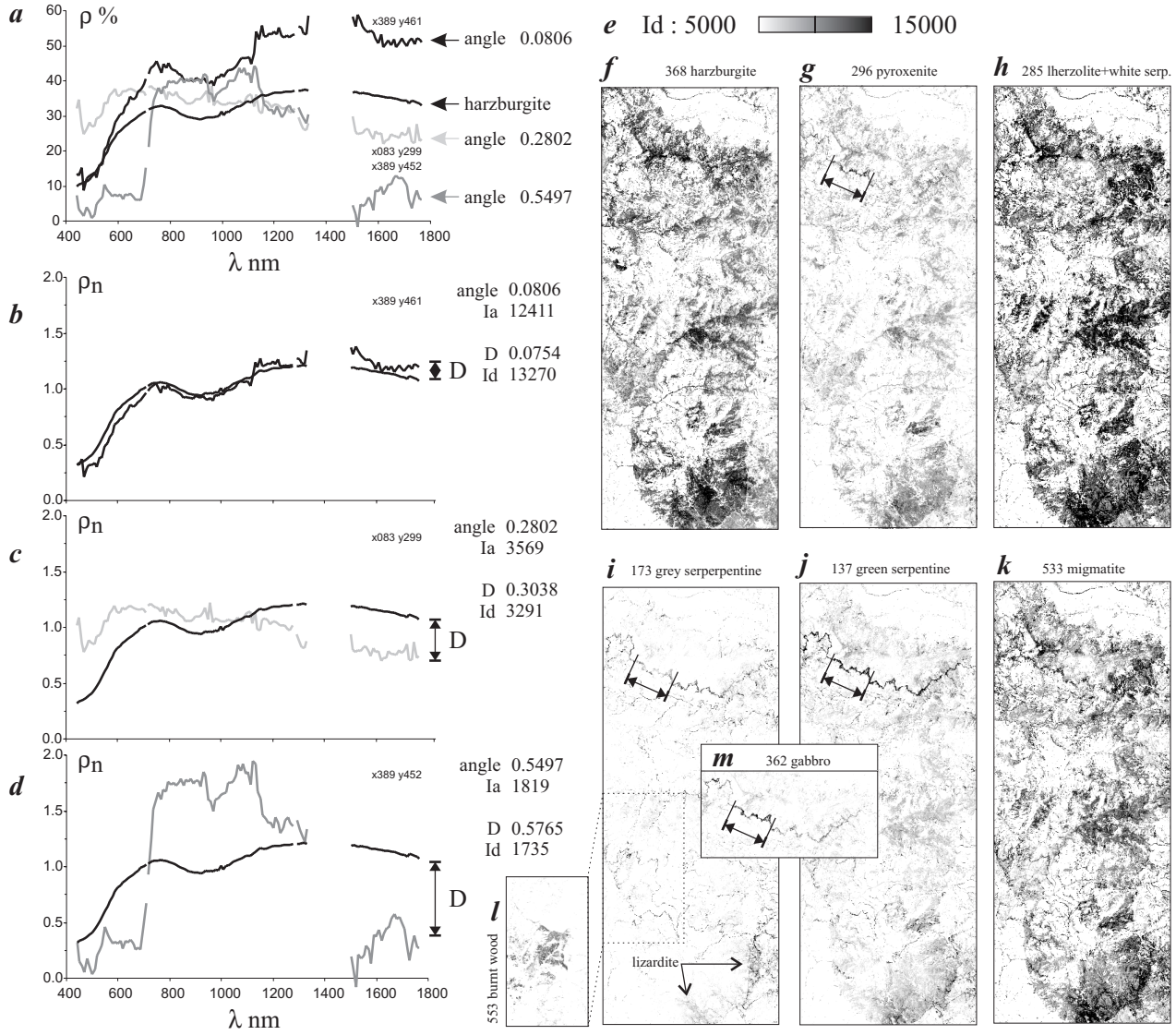

FIG. 9. – Angle mapping and distance between normalised reflectance. ***a***– Reflectance of various pixels compared to field measurements on harzburgite. Angle values between AVIRIS reflectance spectra and the GER3700 field measurements are shown for each pixel. Pixel x389, y461 is peridotite, x083, y299 is serpentine and x389 is pine. ***b***, ***c*** and ***d*** are the normalised reflectance calculated for each pixel and compared to the normalised reflectance of the harzburgite field measurements. The angle is identical to **a** and always close to D, the mean distance between normalised reflectance spectra. ***e***– Greyscale of the Id maps presented in ***f*** to ***l***. The closest pixels to the harzburgite (***b***) are dark in the image (***f***).

FIG. 9. – *"Angle mapping" et distances entre réflectances normalisées.* ***a***– *Réflectance de différents pixels comparées avec des mesures de terrain d'harzburgite. Les angles entre spectres de réflectances AVIRIS et spectres de réflectance GER 3700 de terrain sont représentés pour chaque pixel. Le pixel x389, y461 est une péridotite, x083, y299 est une serpentine et x389 est du pin.* ***b***, ***c*** *et* ***d*** *sont les réflectances normalisées calculées pour chaque pixel et comparées à la réflectance normalisée de la harzburgite mesurée sur le terrain.* ***e***– *Echelle de niveaux gris des cartes d'indice I_d présentées de* ***f*** *à* ***l.*** *Les pixels les plus proches de la lherzolite riche en opx* (***b***) *sont sombres sur l'image* (***f***)

So, they are more often exposed than any peridotite on recent outcrops like roads or streams. The northern road, which is a fresh cut in the peridotite, can be divided in yellow and green sections in figure 10i. However, in the field, the green section is characterised by a low content in magnetite and the yellow section is characterised by a very high content in magnetite. As the chrysotile content seems to remain the same along the road (fig. 9j), it is suggested that the grey serpentine display higher Id intensities in the magnetite rich section because of its magnetite content. On the contrary the pyroxene rich gabbro I_d map (fig. 9l) and the pyroxenite Id map (fig. 9g) display higher intensities along the road sections relatively free of magnetite. The link between the low content of magnetite and the high content of pyroxenes is probably due to the serpentinisation process during which Fe leaves the olivine to form magnetite. When a peridotite is rich in pyroxene, more stable than olivine, there is less Fe available and less production of magnetite, whereas olivine-rich peridotite produces more magnetite. The apparent content in magnetite can therefore change dramatically in peridotite surfaces with its degree of serpentinisation.

An Id map of migmatite rich in plagioclase (> 80 %) is also presented in figure 9k. It displays a surprisingly good match with peridotite, even in areas where there is no plagioclase at all. In the range 400 nm to 1800 nm, it is impossible to distinguish plagioclase from white serpentine in lherzolites (see also fig. 4d and 4f, and discussion in § Field measurement).

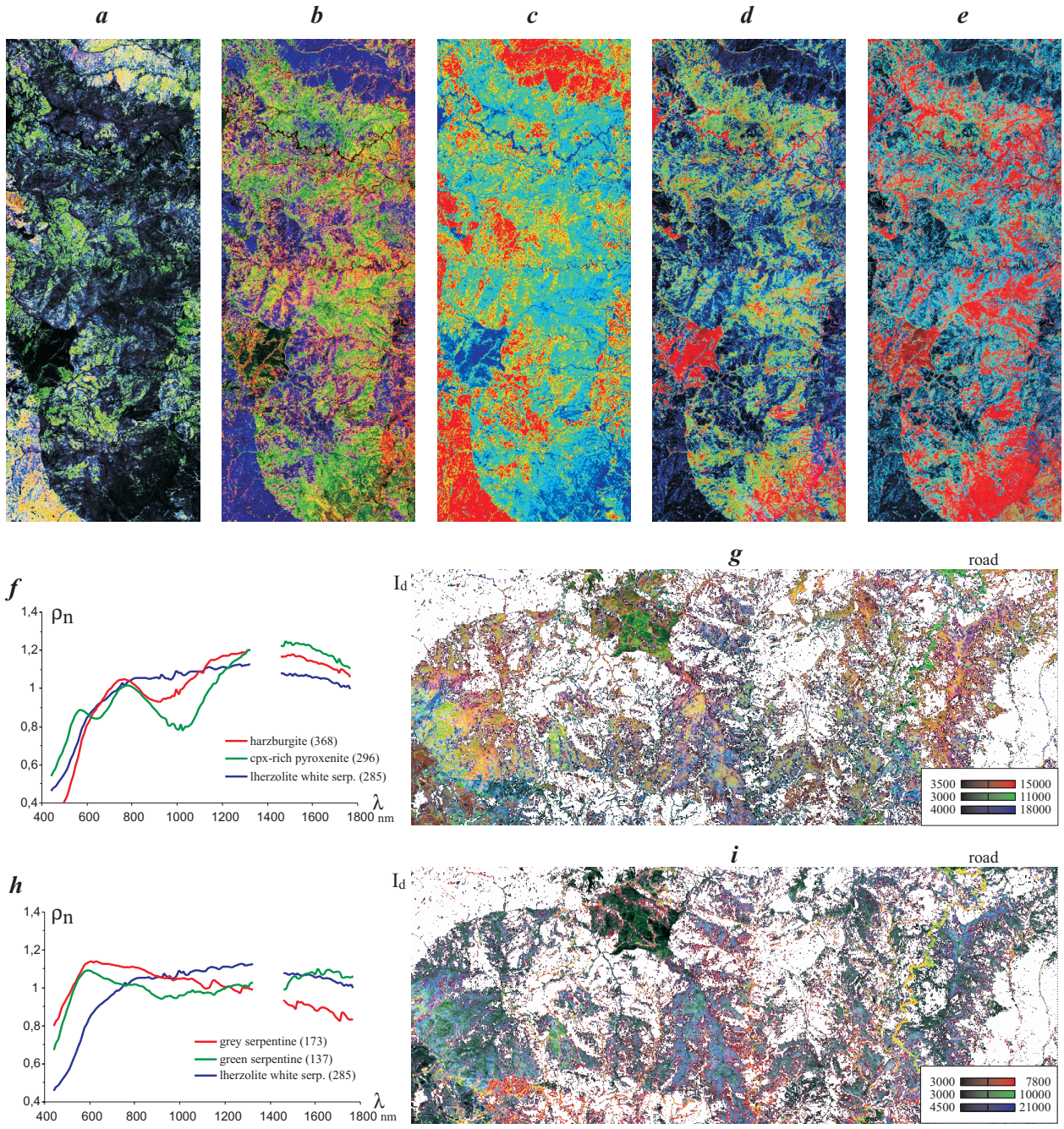

FIG. 10. – RGB (red, green and blue) colour composite images of I_d maps. **a**– I_d maps of oaks, young pines and old pines; **b**– I_d maps of thistle, long grass and lavender; **c**– index of vegetation I_v; **d**– I_d maps of peridotite (harzburgite), grass and thistle; **e**– same colour composite image after grass removal (see § 3.5); **f**– spectra and **g**– I_d maps of harzburgite, pyroxenite and lherzolite with white serpentine; **h**– and **i**– same process for grey serpentine (lizardite with a few magnetite), green serpentine (chrysotile) and lherzolite with white serpentine (lizardite).

FIG. 10. – *RVB (rouge, vert et bleu) compositions colorées des cartes d'indices I_d. a– Carte I_d de chênes, jeunes et vieux pins; b– Carte I_d de chardons, hautes herbes et lavande; c– Indice de végétation I_v; d– Carte I_d de péridotite (harzburgite), herbe et chardon; e– Même image après retrait de l'herbe; **f**– Spectres et g– Carte I_d de harzburgite, pyroxénite et lherzolite à serpentine blanche; h– et i– Même traitement avec des serpentines grises (lizardite avec peu de magnétite), serpentines vertes (chrysotile) et lherzolite à serpentine blanche (lizardite).*

We have shown in this chapter that correlation between field spectra and AVIRIS spectra is possible and allows us to map different geological units. However, one can see that the I_d maps are different from those obtained by Lundeen and Obata [1977 ; fig. 1a] and Darot [1973 ; fig. 1-b], when subtle variations in rock composition are investigated. For example, the content of plagioclase in the peridotite cannot be distinguish from the content of serpentines. We have seen also that fresh cuts of rocks can have different I_d intensities from weathered outcrops, so we can suspect that moderate variation of the outcrop conditions may also induce artificial rock zoning. Future field trips are planned to re-

fine the results of the present remote sensing study. We can however already confirm the zoning of serpentine in the southern part of the massif with the present data.

CONCLUSION

The spectral resolution of AVIRIS images gives the opportunity to combine photo-interpretation of many combinations between its 224 channels and direct spectroscopic analysis at any pixel location.

The photo-interpretation of multiple colour composite images was particularly useful to determine petrographic boundaries between the peridotite and its surrounding rocks, from sandstone, limestone, gneiss and marbles. The important vegetation coverage did not free enough space to map all the limits with automatic techniques. However, the vegetation was useful to outline many boundaries characterised by variations of the vegetation supported by different soils. This work of photo-interpretation was successful in mapping serpentine zoning in Ronda for the first time. This was in part because of a preferential development of thistle-like plants on serpentine. However, confidence in interpreting the colour composite images is due to the ability to compare at each pixel location a full spectrum with field measurements. The characteristic pattern of grey serpentine, which is a mixture of lizardite (white serpentine) and black magnetite, was particularly useful and easy.

The photo-interpretation step was important to define the main components of the massif which are peridotites, serpentines, fire forest, pines, grass and other plants. All these components have to be known prior to any study of internal zoning of the peridotite. Otherwise, by omitting an important component, one could confuse a fire forest impact on peridotite with a mineralogical zoning, or a plagioclase content of the peridotite with a white serpentine content.

We use AVIRIS data from the campaign of 1991, unfortunately limited between 440 nm and 1 800 nm because of technical problems on detector D, and calibrate it with a field measurement in 1997 in the same season, six years later using a GER 3700 spectrometer and a Spectralon® target. The identity between the topographic data and our topography deduced from the atmosphere thickness indicates that our atmospheric correction is valid. Despite the time lapse between both experiments we could remove all the atmospheric absorption features with a comparison of spectra of a white plate (Spectralon®) measured at the bottom and at the top of the massif under the same weather and sun elevation conditions. It was then possible to use angle mapping techniques to study the correlation between spectra of AVIRIS pixels and GER 3700 field measurements. We also defined an index convenient for the display of results in images which can be combined in colour composite images to analyze various petrographic zoning. Because of grass extension over a very large part of the peridotite we also presented a fast algorithm for grass removal by considering that a 400 m^2 pixel is made of many sub-pixels of pure rock and pure vegetation, which is often the case on the Ronda peridotite. This simple algorithm was effective to considerably extend the area of spectral angle mapping. However, the technique has to be improved by using a more precise model of the vegetation cover including topographic information. This will allow us not only to use the angle between field spectra and remote sensing spectra but also to look at the information contained in the intensity.

A few ambiguities have been found between rock types. Some of them are due to a not so selective coverage of the vegetation, like oak trees on either gneiss or migmatites. Some others are due to the inability of the angle mapping techniques to separate spectra of similar shape but differing intensities. This is particularly annoying when the peridotite is enriched in magnetite for example. It is therefore necessary to integrate in our future studies the effect of the topography (roughness and relief) by using bidirectional reflectance studies like Despan *et al*. [1998]. However, the very good agreement found between AVIRIS data and field measurements leads us to expect a better mapping of peridotite types when topography and vegetation contributions would be more completely identified and removed. It also emphasizes the important role of in situ field measurements for any planetary study of rock types.

Acknowledgement. – We thank the *Programme National de Télédétection Spatiale* (INSU-CNRS) which supported the field work. We also thank the *Région des Pays de la Loire* and the *Programme National de Planétologie* (INSU-CNRS) which were the main contributors for the acquisition of the GER 3700 spectrometer shared with the *Laboratoire de Physique & Mécanique des Géomatériaux* (Université de Marne la Vallée). We are also grateful to the reviewers, particularly M. Pubellier and J. M. Tubía whose comments help us to improve a first version of this paper.

References

ADAMS J.B. (1974). – Visible and near-infrared diffuse reflectance spectra of pyroxenes as applied to remote sensing of solid objects in the solar system. – *J. Geophys. Res.*, **79**, 32, 4829-4835.

BIBRING J.-P., ERARD S., GONDET B., LANGEVIN Y., SOUFFLOT A., CARA C., COMBES M., DROSSART P., ENCRENAZ Th., LELLOUCH E., ROSENQVIST J., MOROZ V. I., DYACHKOV A.V., GRIGORIEV A.V., HAVINSON N.G., KHATUNTSEV I.V., KISELEV A.V., KSANFOMALITY L.V., NIKOLSKY Y.V., MASSON P., FORNI O. & SOTIN C. (1991). – Topography of the martian tropical regions with ISM. – *Planet. Space Sci.*, **39**, 225-236.

CARRÈRE V. & CONEL J.E. (1993). – Recovery of atmospheric water vapor total column abundance from imaging spectrometer data around 940 nm-sensitivity analysis and application to airborne visible/infrared imaging spectrometer (AVIRIS) data. – *Remote Sensing Environment*, **44**, 179-204.

CERVELLE B.D. & MAQUET M. (1982). – Cristallochimie des lizardites substituées Mg-Fe-Ni par spectrométrie visible et infrarouge proche. – *Clay Minerals*, **17**, 377-392.

CHABRILLAT S. (1995). – Discrimination lithologique par spectro-imagerie visible-proche infrarouge aéroportée : application au massif péridotitique de Ronda (Espagne). – Dr. Thesis Univ. Toulouse 3, 173 p (ined).

CHABRILLAT S., PINET P.C., CEULENEER G., JOHNSON P.E. & MUSTARD J.F. (2000). – Ronda peridotite massif : methodology for its geologi-

cal mapping and lithological discrimination from airborne hyperspectral data. – *Internat. J. Remote Sensing*, **21**, 2363-2388.

DAROT M. (1973) – Méthodes d'analyse structurale et cinématique. Application à l'étude du massif ultrabasique de la Sierra Bermela (Serrania de Ronda – Andalousie – Espagne). – Dr. Thesis Univ. Nantes, 120 p (ined).

DESPAN D., BEDIDI A., CERVELLE B. & RUDANT J.-P. (1998). – Bidirectional reflectance of gaussian random surfaces and its scaling properties. – *Math. Geol.*, **7**, 873-888.

FARRAND W.H., SINGER R.B. & MERÉNYI E. (1994). – Retrieval of apparent surface reflectance from AVIRIS data : A comparison of empirical line, radiative transfer, and spectral mixture methods. – *Remote Sensing Environment*, **47**, 311-321.

GAO B.C., HEIDEBRECHT K.B. & GOETZ A.F.H. (1993). – Derivation of scaled surface reflectances from AVIRIS data. – *Remote Sensing Environment*, **44**, 165-178.

GREEN R.O., CARRERE V. & CONEL J.E. (1989). – Measurement of atmospheric water vapour using the airborne visible/infrared imaging spectrometer. – Image Processing '89*, Am. Soc. Photogramm. Remote Sens.* (ASPRS).

HIROI T. & PIETERS C.M. (1994). – Estimation of grain sizes and mixing ratios of fine powder mixtures of common geologic minerals. – *J. Geophys. Res.*, **99**, 10867-10879

ELVIDGE C.D., CHEN Z. & GROENEVELD D.P. (1993). – Detection of trace quantities of green vegetation in 1990 AVIRIS data. – *Remote Sensing Environment*, **44**, 271-279.

JACQUEMOUD S. (1993). – Inversion of the PROSPECT + SAIL canopy reflectance model from AVIRIS equivalent spectra : theoretical study. – *Remote Sensing Environment*, **44**, 281-292.

KING T.V.V. & CLARK R.N. (1989). – Spectral characteristics of chlorites and Mg-serpentines using high-resolution reflectance spectroscopy. – *J. Geophys. Res*, **94**, no. b10, 13997-14008.

KRUSE F.A. (1988). – Use of airborne imaging spectrometer data to map minerals associated with hydrothermally alterated rocks in the northern Grapevine Mountains, Nevada, and California. – *Remote Sensing Environment*, **24**, 31-51.

KRUSE F.A., KIEREIN-YOUNG K.S. & BOARDMAN J.W. (1990). – Mineral mapping at Cuprite, Nevada with a 63-channel imaging spectrometer. – *Photogramm. Eng. Remote Sens*. **56** (1), 83-92.

KRUSE F.A., LEFKOFF A.B., BOARDMAN J.W., HEIDEBRECHT K.B., SHAPIRO A.T., BARLOON P.J. & GOETZ A.F.H. (1993). – The spectral image processing system (SPIS) – interactive visualization and analysis of imaging spectrometer data. – *Remote Sensing Environment*, **44**, 145-163.

LUNDEEN M.T. & OBATA M. (1977). – Geologic map of the Ronda ultramafic complex, southern Spain. – The Geological Society of America, Inc. © *1979*, Map and chart series MC-29.

MUSTARD J.F. & PIETERS C. (1989). – Photometric phase functions of common geological minerals and applications to quantitative analysis of mineral mixture reflectance spectra. – *J. Geophys. Res.*, **94**, no. b10, 13619-13634.

NICOLA A. (1986). – Structure and petrology of peridotites : clues to their geodynamic environment. – *Rev. Geophys.*, **24**, 875-895.

OBATA M. (1980). – The Ronda peridotite : garnet-, spinel-, and plagioclase-lherzolite facies and the P-T trajectories of high temperature mantle intrusion. – *J. Petrol.*, **21**, 533-572.

PIETERS C.M. & ENGLERT P.A.J. (1993). – Remote geochemical analysis : elemental and mineralogical composition. – Published by Cambridge University Press ; Topics in Remote Sensing, 4, ISBN 0521402816.

RICHARDS J.A. (1994). – Remote sensing digital image analysis : An introduction. – Second, revised and enlarged edition. – Springer-Verlag Berlin, 340 pp.

ROBERTS D.A., YAMAGUSHI Y. & LYON R.J.P. (1986) – Comparison of various techniques for calibration of AIS data. *In* : G. VANE and A.F.H. GOETZ, Eds Proc. *2nd Airborne Imaging Spectrometer Data Analysis Workshop*.

ROBERTS D.A., GREEN R.O. & ADAMS J. B. (1997). – Temporal and spatial patterns in vegetation and atmospheric properties from AVIRIS. – *Remote Sensing Environment*, **62**, 223-240.

SÁNCHEZ-GÓMEZ M., GARCÍA-DUEÑAS V. & MUÑOZ M. (1995). – Relations structurales entre les péridotites de la Sierra Bermeja et les unités alpujarrides sous-jacentes (Benahavís, Ronda, Espagne). – *C. R. Acad. Sci.,* Paris, 321, 885-892.

SINGER R.B. (1981). – Near-infrared spectral reflectance of mineral mixtures : systematic combinations of pyroxenes, olivine, and iron oxides. – *J. Geophys. Res*., **86**, 7967-7982.

SÁNCHEZ-RODRÍGUEZ L. & GEBAUER D. (2000). – Mesozoic formation of pyroxenites and gabbros in the Ronda area (southern Spain), followed by early Miocene subduction metamorphism and emplacement into the middle crust : U-Pb sensitive high-resolution ion microprobe dating of zircon. – *Tectonophysics*, **316**, 19-44.

TUBÍA J.M. & CUEVAS J. (1986). – High-temperature emplacement of the Los Reales peridotite nappe (Betic Cordillera, Spain). – *J. Struct. Geol.*, **8**, 473-482.

TUBÍA J.M., CUEVAS J., NAVARRO-VILÁ J., ALVAREZ F. & ALDAYA F. (1992). – Tectonic evolution of the Alpujarride complex (Betic Cordilleras, southern Spain). – *J. Struct. Geol.*, **14**, 193-203.

TUBÍA J.M., CUEVAS J. & GIL IBARGUCHI J.I. (1997). – Sequential development of the metamorphic aureole beneath the Ronda peridotites and its bearing on the tectonic evolution of the Betic Cordillera. – *Tectonophysics*, **279**, 227-252.

VAN DER MEER F. (1996). – Metamorphic facies zonation in the Ronda peridotites : spectroscopic results from field and GER imaging spectrometer data. – *Internat. J. Remote Sensing*, **17**, 9, 1633-1657.

VAN DER WAL D. (1993). – Deformation processes in mantle peridotites, with emphasis on the Ronda peridotite of SW Spain. – Ph. D. Thesis Univ. Utrecht, 180 p.

VAN DER WAL D. & VISSERS R.L.M. (1996). – Structural petrology of the Ronda peridotite, SW Spain : deformation history. – *J. Petrol*, **37**, 23-43.

VANE G., GREEN R. O., CHRIEN T.G., ENMARK H. T., HANSEN E.G. & PORTER W.M. (1993). – The airborne visible/infrared imaging spectrometer (AVIRIS). – *Remote Sensing Environment*, **44**, 127-143.